Paper 148

CFD ADAPTIVE MESH REFINEMENT FOR ROTORCRAFT WAKE SIMULATIONS

Mark Potsdam, Andrew Wissink, Sean Kamkar
mark.potsdam@us.army.mil, andrew.m.wissink@us.army.mil, skamkar@merlin.arc.nasa.gov
US Army Aeroflightdynamics Directorate (AMRDEC), Moffett Field, CA, USA

Buvana Jayaraman
buvana.jayaraman@us.army.mil
Science and Technology Corp., Moffett Field, CA, USA

ABSTRACT

The multidisciplinary Helicopter Overset Simulation software (Helios) is applied to study adaptive mesh refinement (AMR) for rotorcraft wake simulations. Near-field and off-body meshes are investigated to determine the effects of refinement level on wake development. It is seen that both regions of the flow field must be resolved for accurate predictions. Unsteady AMR is used in the off-body with a Cartesian mesh adaption scheme. Different adaption criteria (vorticity, Q-criterion, and normalized Q-criterion) are explored. Normalized Q-criterion and a vorticity estimate based on physical rotor parameters provide a threshold estimate which does not require a priori knowledge of the flow field, thus aiding automated implementation of AMR in a production environment. AMR is shown to provide a significant reduction in cost compared with fixed refinement, while enabling improved wake tracking and interactional aerodynamics. Application of AMR for several rotorcraft configurations across a range of flight conditions, including high speed, low speed, descending flight blade-vortex interaction, and hover are shown.

1 INTRODUCTION

Vortical wakes introduce important aerodynamic phenomena in various aerospace vehicles. Rotary-wing aircraft, in particular, fly in their own wake and experience numerous aeromechanic interferences which affect vehicle performance, handling qualities, vibration, and noise. The wake also complicates near-ground operations, from shipboard landings to “brownout” conditions in desert operations. The availability of accurate and efficient computational models to better predict vortical wake behavior could help to minimize the onset of these disruptive and costly phenomena.

High-fidelity Reynolds-Averaged Navier-Stokes (RANS) CFD methods have demonstrated the ability to give accurate predictions of near-field aerodynamic loads, but their ability to predict the far-field wake is often limited by numerical dissipation. This can be mitigated by using very fine grids, but available computational resources can quickly be exhausted. For problems where key solution features, like tip vortices, occur only in localized regions of the computational domain, spatial adaptive mesh refinement (AMR) can be an effective tool. AMR involves automatically refining and coarsening the grid locally to resolve important flow and geometric features, i.e. feature-based adaption. By focusing computational effort in these localized regions, a highly resolved solution may be obtained much more economically than a globally refined grid of equal resolution.

The use of AMR has been studied extensively for wakes of hovering rotors. Strawn and Barth [1] demonstrated the concept using AMR in an unstructured Euler solver. Kang and Kwon [2] applied a similar strategy within an unstructured Navier-Stokes solver. These and other efforts all adopted AMR techniques targeting steady-state solutions, such as hovering rotors, with the adaption typically being performed as an off-line procedure.

However, many of the more complex problems in rotorcraft aeromechanics require time-dependent, moving body capability. A scheme that can resolve unsteady effects like rotor-fuselage interactions or rotor vehicles in forward flight or maneuver conditions requires an *unsteady* AMR approach, in which the grid is adapted continually in a time dependent manner throughout the simulation. An intermediate step to fully unsteady AMR involves tracking and recording features and then adapting only on a periodic basis, such as the rotor rotation frequency. In this fashion, Yu and Kwon [3] investigated blade-vortex interaction with adaptive unstructured meshes. Shenoy and Smith [4] investigated rotor-fuselage interaction using unstructured, overset meshes.

In a fully unsteady AMR effort, Dietz et al. [5] introduced an overset grid approach that moved and deformed tubular curvilinear grids to align with the tip vortices. Meakin [6] developed a Cartesian grid AMR scheme within the OVERFLOW-D code. Wissink and Sitaraman et. al [7,8] developed and validated AMR in the Helios flow solver using the SAMRAI unsteady AMR package for rotorcraft in hover and forward flight. Buning [9] implemented an efficient unsteady AMR methodology in OVERFLOW, and it has been demonstrated for rotors in hover [10] and forward flight.

The AMR procedures applied to rotorcraft problems to date use geometry- and solution-based feature adaption methods. Promising techniques based on the adjoint equations have seen use on steady fixed wing configurations and for rotor design in hover [11]. The adjoint-based methodology has not yet been fully applied to unsteady rotorcraft

configurations for feature detection, as the unsteady aspects add considerable complexity and cost.

Another important strategy for CFD-based wake resolution is the use of high-order numerics. High-order schemes are effective because they resolve features like tip vortices with much fewer points across the vortex core. Analysis of higher-order central difference schemes has shown that every two order of magnitude increase in the numerical methods can halve the number of points required to resolve and convect a vortex with minimal dissipation [12]. As such a 5^{th}-order scheme was seen to need 8 points across the vortex core diameter, while a 2^{nd}-order scheme required 30. The benefits of high-order schemes, including finite difference and discontinuous Galerkin (DG) methods, for rotor wakes have been well documented by Hariharan [13], Yeshala [14], Nastase [15], and Chen [16].

The objectives of this work are to investigate the details regarding off-body adaptive mesh refinement (AMR) for rotorcraft wake flow fields. How the relevant parameters of feature-based adaption, such as refinement criteria, adaption threshold, and buffer regions, might affect the AMR meshes, solution accuracy, and numerical efficiency will be studied. Feature-based adaption methods which do not require a priori knowledge of the flow field are sought. Tip vortex development will be shown in the context of the need for near-body AMR. Test cases across a wide range of rotorcraft flight conditions and for several geometric configurations will be used to illustrate the advantages and deficiencies of AMR.

Section 2 briefly discusses the Helios computational methodology used in this work. Section 3 gives an overview of the configurations and computational geometries which are studied. Section 4 discusses application details of near- and off-body adaptive mesh refinement, including appropriate adaption criteria. Section 5 shows specific examples of issues related to adaption for a range of rotorcraft flight conditions. The findings of the work are summarized in the Conclusions.

2 Helios COMPUTATIONAL METHODOLOGY

2.1 Software Infrastructure Framework (SIF)

The HELIcopter Overset Simulations software (Helios) is a multi-disciplinary computational platform that includes software components responsible for near-body and off-body CFD, domain connectivity, rotorcraft comprehensive analysis, mesh motion and deformation, a fluid-structure interface module and a fluid-flight-dynamics interface module [17]. Helios uses a flexible and lightweight Python infrastructure, referred to as the Software Integration Framework (SIF), to control their combined operation and data exchanges. Figure 1 shows a schematic representation of SIF. It is comprised of a series of Python scripts that communicate with and execute the different software components.

The basis of the Helios aerodynamics solution procedure is a dual-mesh paradigm that consists of unstructured meshes in the near-body region and Cartesian meshes in the off-body region (Figure 2). The unstructured meshes allow ease of grid generation for complex configurations while ensuring proper resolution of the boundary layer region. The Cartesian meshes enable the use of efficient high-order spatial discretizations and adaptive mesh refinement (AMR) to accurately resolve the off-body flow structures. The two mesh systems transfer data using an overset domain connectivity formulation that is responsible for interpolating the solution data between them. The overset procedure facilitates the relative motion between the mesh systems. The unstructured near-body meshes move and deform with the geometric surface, while the background Cartesian off-body meshes remain stationary.

2.2 Near-body Unstructured CFD

The near-body CFD solver in Helios is the NSU3D code [18], which is a Reynolds-Averaged Navier-Stokes (RANS) code capable of handling arbitrary unstructured mesh elements. NSU3D utilizes a node-centered, finite volume scheme, that is spatially 2^{nd}-order accurate. The scheme is also 2^{nd}-order accurate in time, employing a backward Euler formulation along with dual time-stepping for iterative convergence at each physical time step. The implicit solution scheme is comprised of a non-linear multigrid algorithm that employs a multi-stage Runge-Kutta scheme with line-Jacobi relaxation as a smoother at each grid level. The Spalart-Allmaras turbulence model is used in the near-body unstructured mesh.

2.3 Off-body Cartesian CFD

The Cartesian off-body solver in Helios is referred to as SAMARC [19], which is a combination of the block structured meshing infrastructure SAMRAI [20] and the ARC3DC solver [21], which solves the inviscid Euler equations and is optimized for isotropic Cartesian grids. As such it is computationally fast and has low memory overhead. The CFD solver uses an temporally 3^{rd}-order explicit Runge-Kutta time integration scheme and a 5^{th}-order spatially accurate central difference scheme with scalar artificial dissipation. The SAMRAI meshing infrastructure provides the ability to adaptively refine the Cartesian mesh system. It is fully automatic, parallel and robust.

2.4 Domain Connectivity

The domain connectivity formulation in Helios is provided by the Parallel Unsteady Domain Information Transfer (PUNDIT) component [22]. It provides fully automated domain connectivity support in parallel, distributed computing systems. Salient features of PUNDIT are: (1) an implicit fringe determination strategy, i.e., the fringes are not explicitly specified, (2) implicit hole cutting, i.e., the grids with the best resolution are used for flow solution, while all other overlapping grid cells are interpolated, and (3) minimum hole cutting using ray tracing for cutting holes in the mesh to accommodate solid bodies.

2.5 Adaptive Mesh Refinement (AMR)

Off-body mesh refinement is a key component of Helios. The SAMRAI package [20] from Lawrence Livermore National Lab manages the construction of the mesh and parallel MPI-based communication between blocks. SAMRAI is an object-oriented C++-based framework that provides an extensible and scalable infrastructure for parallel AMR applications.

The unsteady AMR strategy is based on the structured AMR ideas of Berger, Colella, and Oliger [23]. The block structured Cartesian grid system is composed of a hierarchy of nested refinement levels, with each level formed as a union of logically-rectangular grid regions. The coarsest level defines the physical extent of the computational domain and each finer level is successively formed automatically by selecting cells on the coarser level and clustering the tagged cells together to form block regions constituting the new finer level. The ratio of mesh spacing between levels is a factor of 2.

The criteria used to select cells for refinement is dependent on both solution-based quantities as well as geometry proximity considerations. Geometry-based refinement applies to those off-body cells that lie close to or overlap the near-body mesh (Figure 3a). In this case tagging and refinement proceeds until the off-body cell size matches the resolution of the near-body mesh. Ensuring cell size compatibility between near-body and off-body cells has important accuracy implications for the overset formulation. Cells which contain flow features that require resolution, such as regions of high vorticity, are tagged for solution-based refinement (Figure 3b-c).

The SAMRAI feature-based adaption procedure has the disadvantage of requiring user input for the threshold value of the adaption criterion, which is frequently not known without experimentation. Recent developments can also utilize an automated feature detection approach which is available in the Guided Adaptive Mesh Refinement (GAMR) module [24]. In this case, the adaption function is normalized so that the threshold value is problem invariant and, consequently, no user tuning is necessary.

Independent of the refinement scheme, some adjustable parameters can help guide the construction of the off-body AMR grid system. A user-specified tag buffer, which extends the tagged region a specified number of surrounding cells, is beneficial for unsteady problems where solution features tend to migrate. If a finer grid is constructed only around regions where the feature is located, by the time the solution advances, the feature may move into coarser grids where it will dissipate. The tag buffer effectively extends the fine mesh region around the feature, preserving the feature in the fine mesh until the next adaptation cycle. The size of the tag buffer is related to the adapt frequency; a small tag buffer is useful when there is frequent adaptation, whereas a large tag buffer is needed if adaptation is less frequent. The adapt frequency is also a user-defined parameter, which should be commensurate with the convective scales and geometric movement of the problem as well as the finest mesh spacing employed.

3 CONFIGURATIONS

3.1 UH-60A Black Hawk

An extensive flight test database exists for the UH-60A Black Hawk helicopter in level flight and transient maneuvers [25]. The flight test data were obtained during the NASA/Army UH-60A Airloads Program. The database provides aerodynamic pressures, structural loads, control positions, and rotor forces and moments, allowing for the validation of both aerodynamic and structural models. The test matrix contains a range of advance ratios and gross weight coefficients. Numerous investigators have used this extensive database for coupled computational fluid dynamics and computations structural dynamics (CFD/CSD) validation.

Several flight conditions are investigated in order to validate the AMR functionality. The test cases are detailed in Table 1. Each flight condition has distinct and noteworthy features, and almost all have been widely studied in the literature [e.g. 8,26,27] with comparisons between test data and CFD/CSD results. Test counter c8534 is a high speed condition with advancing blade three-dimensional transonic effects and negative blade tip loading. C8513 and c8515 are low speed conditions with high vibration and strong blade-wake interactions involving the super-vortex. C8515 has a lower advance ratio of 0.11 and is investigated here for rotor-fuselage interaction. C9017 is a high thrust coefficient case with retreating blade dynamic stall. C9812 is a descending flight condition with significant blade-vortex interaction (BVI).

Table 1. UH-60A flight conditions

counter	advance ratio	C_T/σ	AOA (deg)
c8534	0.37	0.084	-7.31
c8513	0.15	0.076	+0.75
c8515	0.11	0.078	+0.87
c9812	0.15	0.065	+5.81
c9017	0.24	0.126	-0.19

Two near-body unstructured meshes have been generated for the UH-60A configuration (Figure 4) using GRIDGEN surface and AFLR volume grid generation software. The coarse mesh contains 1.1 million nodes per blade, while the fine mesh has 3.9 million. In addition to being twice as fine on the surface, the fine mesh also includes clustering in the volume grid around the blade tip. Due to the reduced spacing in the volume grid, it is also possible with regard to off-body mesh overlap to move the near-body outer boundary closer to the solid surface. For the off-body Cartesian grids, 6, 7, 8, and 9 levels of resolution are employed, corresponding to 20, 10, 5, and 2.5% chord spacing in the wake, respectively. The meshes are detailed in reference [8].

3.2 Tiltrotor Aeroacoustics Model (TRAM)

The Tilt Rotor Aeroacoustics Model (TRAM) is an extensive wind tunnel model constructed to facilitate tiltrotor aeromechanics research. The geometry is a 0.25-scale V-22 right-hand nacelle and 3-bladed rotor. The isolated TRAM rotor was tested in the Duits-Nederlandse Windtunnel Large Low-speed Facility (DNW-LLF) in the spring of 1998 [28]. It provides a significant source of aeroacoustics, performance, and structural loads data for validation of tiltrotor analyses. Among the aerodynamics data acquired were rotor performance and blade pressures. Hover runs were performed at a nominal tip Mach number of 0.62.

Two unstructured near-body meshes have been generated for this configuration as well. The coarse mesh contains 0.9 million nodes per blade, while the fine mesh has 3.1 million nodes per blade with manual grid clustering and refinement around the outer portion of the blade. For the off-body, a finest level spacing of 5% tip chord is used. The computational meshes and hover performance predictions, including the use of AMR, are detailed in reference [7].

4 NUMERICAL INVESTIGATIONS

4.1 Near-body Adaption

Much of the focus of AMR applications to rotorcraft targets off-body refinement, however, it is instructive to first investigate near-body resolution and adaption in the context of the effect it has on off-body wake adaption. Helios currently has no capability for automated unstructured mesh adaption, so in this effort refinement has been performed manually in the grid generation phase. Node clustering is based on a priori knowledge of the flow field. This includes taking into account tip vortex development in hover and forward flight and returning vortex blade passing miss distance in hover.

Near-body unstructured mesh adaption capability does exist for the NSU3D Helios module as an off-line process for steady calculations. It has been demonstrated for both on-surface and wake refinement for fixed-wing and rotary-wing (non-inertial) configurations [29,30]. The key capabilities for future efforts in this area are to perform the unstructured mesh adaption in parallel at runtime for unsteady calculations. However, unstructured meshes make on-the-fly surface point insertion, anisotropic adaption for viscous grids, mesh repartitioning, load balancing, and solution interpolation in a parallel environment much more demanding than the Cartesian mesh counterpart.

The near-body mesh is responsible for the development and initial roll-up of the tip vortex, so it is important that this flow feature be resolved and transitioned accurately to the off-body mesh in an overset environment. Spacing compatibility between meshes is a key tenet of overset grid generation. Figure 5 shows the near-field tip vortex formation and roll-up emanating from the 0 deg azimuth blade of the UH-60A in high speed flight (c8534) using coarse (Figure 5a) and fine (Figure 5b) near-body meshes. The tip vortex, shown as an iso-surface of vorticity, is well defined in this top view of the rotor blade tip. Focusing on the unstructured part of the iso-surface, it is clear that the vortex in the fine grid is much tighter than in the coarse grid. This is also a consequence of the larger extent of the unstructured region in the coarse near-body grid (Figure 4c), compared to the fine near-body grid outer boundary which has been cut back (Figure 4d). The extent of the outer boundary is partially dictated by the spacing in this overlap region. The coarser mesh shows a significant increase in core size compared with the fine mesh. It may be obvious to state, but regardless of the accuracy of the off-body scheme, it cannot reverse the dissipation which occurred in the near-body region (vorticity confinement not withstanding).

Figure 5b-d investigates the effect of off-body spacing on the tip vortex near-field. Three off-body spacings – 10, 5, and 2.5% chord – are shown. The coarse mesh (Figure 5a) uses 20% chord off-body spacing. The 5% chord spacing (Figure 5c) is consistent with the volume spacing in the fine unstructured grid and shows a reduced tip vortex size compared with 10% chord spacing (Figure 5b). Based on the 5^{th}-order numerical scheme 8-10 points are required to capture and convect a tip vortex, such that the 10% chord grid is known to be insufficient. On the other hand, the 2.5% chord grid (Figure 5d) shows little improvement in tip vortex structure and long distance convection capability. Because of the spacing incompatibility with the near-body, the smallest off-body spacing is excessive and inefficient in this case. In all plots, the vortex formation in the near-body grid appears to be unaffected by the subsequent off-body spacing.

A similar analysis is performed for the TRAM rotor solution in hover [7]. Figure 6a-b shows the coarse and fine near-body meshes, respectively. The coarse mesh displays a drastic increase in tip vortex size due to the lack of refinement in the near-body mesh (Figure 6c). The vortex size is seen to be maintained past the first blade passing by the high-order off-body mesh, but is nonetheless too large because of the incorrect initial generation at the blade tip. Note that the near-body mesh region can be discerned by the somewhat unsmooth iso-surface in this figure. In contrast, the fine mesh, which includes manual grid clustering at the blade tip and first blade passage (Figure 6b), shows a significantly reduced vortex core size at the tip and consequently at the first blade passage (Figure 6d). The subsequent tip vortices in the wake are also better resolved due to the more accurate initial generation (Figure 6e-f). Note that the off-body meshes in both cases use exactly the same AMR resolution, so the differences can be isolated solely to being caused by the near-body mesh resolution and refinement.

As a third example, Helios was used for investigation of the Higher Harmonic Control Aeroacoustics Rotor Test (HART) II blade-vortex interaction configuration [31]. The HART II test is a widely-used comprehensive wind tunnel database for acoustics and higher harmonic control investigations. The test was conducted in the German-Dutch Wind

tunnel (DNW) using a 40% Mach-scaled Bo105 model rotor in descending flight. That study confirmed the importance of near-body resolution and refinement as a driver for off-body wake capturing. When a coarse near-body grid was employed, increasing the off-body resolution had a trivial effect on the airloads predictions, as the near-body was the limiting factor.

All these investigations (UH-60A, TRAM, HART II) indicate that in spite of the extensive efforts over the past decade to develop accurate off-body schemes that can convect vortices for long distances with minimal dissipation, they are still dependent on the near-body initial vortex generation and development. This needs to be remembered when considering off-body rotorcraft wake flow fields. Future efforts should see more focus on adaptive methods and high-order numerical for grid topologies that can handle complex geometry and viscous effects, such as the unstructured meshes used here and curvilinear structured grids used in the literature.

4.2 Off-body Adaption

Feature-based adaption in the off-body mesh is investigated here. In all cases, an initial fixed refinement solution has been obtained and the off-body Cartesian grid spacing is 5% chord. The fixed refinement covers a rectangular region surrounding the rotor and encompassing the wake in hover or forward flight to some extent downstream. To test the adaption scheme, the fixed refinement grid and well converged solution is used as the starting point. One adaption cycle is run based on this solution with the particular parameters being investigated. The specific adaption methodology then identifies only relevant regions out of the fixed refinement, and uses the same maximum refinement level. Using this methodology, various refinement criteria can be consistently compared and the adaption efficiency versus fixed refinement determined. Adaption efficiency is defined as the ratio of the AMR point count compared with fixed refinement, N_{AMR}/N_{fixed}. Lower numbers are better. In all the figures showing Cartesian grids, only every other point is typically shown for clarity.

The UH-60A high speed case (c8534) is a reasonable flight condition for testing adaption criteria because it contains important tip vortex features as well as prominent shear layers, root vortices, and vortices emanating from the swept tip break. The tip vortices are strongest on the 0 and 270 azimuth blades. The advancing blade is well known to have negative lift at the tip which can generate an opposite sense tip vortex. In general the vortical structure in the 2nd quadrant is indistinct and is dominated by the wake sheet on the outboard part of the blade. A super-vortex is generated on the advancing side of the rotor, but does not appear on the retreating side. Because of the high advance ratio, the helical vortex structures are spaced relatively far apart which allows for more distinct regions for AMR to identify. In hover the tip vortices are more closely spaced than in forward flight.

4.2.1 Vorticity-based Adaption

The most common refinement criteria for rotorcraft wakes has been vorticity magnitude, as seen in the references cited in the Introduction. Vorticity-based refinement for a range of non-dimensional vorticity levels is shown in Figure 7 for the UH-60A. The grid through the hub at z = 0 is shown. Flow is from left to right. Vorticity (ω) is non-dimensionalized by a reference length and speed of sound for the ARC3DC flow solver. Figure 7a shows the fixed refinement grid extent along with vorticity contour levels. The adapted grids generated based on different vorticity thresholds are shown in Figure 7b-f and detailed in Table 2. Compared with fixed refinement, reasonable adaption levels (ω = 0.0025-0.0065) require only 20-40% of the number of grid points for the same refinement level. Choosing a refinement threshold which is too low results in an adapted region that covers most of the wake, although even for a vorticity level of 0.00045, a 50% grid point reduction is realized. For a very low value of 0.00010 (Table 2) the grid point count actually increases relative to fixed refinement due to overhead associated with overlapped grids.

For flight conditions at different advance ratios, the point count saving is approximately the same as long as the adaption threshold, ω_{adapt}, is scaled by the thrust coefficient. Results are illustrated in Table 3, where a constant value of $(C_T/\sigma)/\omega_{adapt}$ produces a constant AMR efficiency (N_{AMR}/N_{fixed}). This is not a completely intuitive finding as it might be expected that the additional wake turns contained in the rotor disk at lower advance ratio or the increase in number of other flow structures such as separation at high thrust coefficient would make the AMR in these conditions less efficient, with more of the fixed region being tagged. When the adaption threshold is not scaled by C_T, the c9017 case shows reduced AMR efficiency (0.37) while the c8513 case shows higher efficiency (0.27), such that in general no clear trend can be discerned based on advance ratio.

Table 2. UH-60A vorticity-based AMR meshes

vorticity (ω)	AMR grid points (M)	N_{AMR}/N_{fixed}
fixed	149.5	1.00
.00010	156.8	1.05
.00045	80.9	0.54
.0025	53.1	0.36
.0045	41.3	0.28
.0065	33.9	0.23
.0135	23.8	0.16

Table 3. UH-60A AMR efficiency with advance ratio

counter	advance ratio	C_T/σ	ω_{adapt}	$\frac{C_T/\sigma}{\omega_{adapt}}$	AMR grid points (M)	N_{AMR}/N_{fixed}
8513	0.15	.076	.0040	19.0	44.4	0.30
9017	0.24	.126	.0068	18.5	43.4	0.30
8534	0.37	.084	.0045	18.7	43.3	0.30

Table 4. TRAM hover vorticity-based AMR meshes

vorticity (ω)	AMR grid points (M)	N_{AMR}/N_{fixed}
fixed	105.0	1.0
0.0010	61.2	0.58
0.0025	49.2	0.47
0.0038	43.2	0.41
0.0050	38.1	0.36
0.0062	35.1	0.33
0.0087	30.9	0.29
0.0100	29.3	0.28
0.0150	25.2	0.24

A vorticity-based threshold study was also performed for the TRAM rotor in hover. Details of the AMR meshes are shown in Table 4. Figure 8 shows the meshes for a coordinate slice at y = 0 along with the fixed refinement mesh indicating vorticity contours. It is seen that the tip vortices are distinct and the hub wake, root vortices, and blade shear layers are identifiable. The AMR grid efficiency is similar to the UH-60A simulations, on the order of 30-45%, across a wide range of reasonable vorticity thresholds (ω = 0.0025-0.01). The wake shear layers can only be captured at the lowest threshold levels (ω < 0.0025).

A disadvantage of feature-based refinement on physical quantities, such as vorticity, is the requirement for the user to specify the adaption threshold. Typically this requires a solution in advance, possibly with a fixed refinement mesh approach. This solution must then be interrogated to obtain the appropriate adaption level for the features desired. As shown above for the UH-60A and TRAM, vorticity values in a reasonable range can be found that result in AMR meshes which capture the relevant flow features (vortices, wakes, shear layers) without excessively refining regions of non-interest and still resulting in significant efficiencies. In previous Helios rotorcraft calculations using AMR [7,8,31], values were chosen based purely on interrogation of the wake with post-processing visualization software, examination of vorticity iso-surfaces, and user expertise, along with trial and error.

4.2.1.1 A Priori Vorticity Threshold Estimate

If basic assumptions are made about rotorcraft flow fields, it may be possible to determine an adaption criteria a priori: 1) The tip vortex is the key feature of interest. 2) The rotor system is a lifting body and the bound circulation is the dominant mechanism for vorticity generation. 3) With known flight conditions, an estimate of the rotor trim parameters (i.e. thrust) is available. None of these assumption can be met for more arbitrary configurations such as the shed vorticity behind a blunt body (cylinder, fuselage, hub), so that the following development would require additional development for such complex configurations.

For an ideal rotor in hover with a uniform circulation (linear lift) distribution along the span, the constant bound circulation, Γ, is [32]

$$\Gamma = 2\Omega R c \left(\frac{C_T}{\sigma}\right) \tag{1}$$

where Ω is the rotor rotation speed (rad/sec), R is the rotor radius, c is the mean blade chord, C_T is the thrust coefficient, and σ is the rotor solidity, $N_b c/\pi R$. The swirl velocity, v_θ, in the tip vortex can be approximated by a Lamb-Oseen vortex [32]

$$v_\theta(r) = \frac{\Gamma_v}{2\pi r_c \bar{r}}\left(1 - e^{-\alpha \bar{r}^2}\right) \tag{2}$$

where $\bar{r} = r/r_c$, r is the radial coordinate of the vortex, r_c is the vortex core radius where the swirl velocity is maximum, and α is 1.25643. The stream-wise vorticity associated with such a vortex is

$$\omega_z = \frac{1}{r}\frac{\partial (r v_\theta)}{\partial r} = \frac{\Gamma_v}{\pi r_c^2}\alpha e^{-\alpha \bar{r}^2} \tag{3}$$

Substituting Equation 1 for the vortex circulation, Γ_v

$$\omega_z = \frac{2\Omega R c}{\pi r_c^2}\left(\frac{C_T}{\sigma}\right)\alpha e^{-\alpha \bar{r}^2} \tag{4}$$

Table 5. AMR vorticity adaption parameters: ω_{adapt}: manually selected threshold for AMR calculation, ω_{AMR}: a priori threshold estimate, K: $\omega_{adapt}/\omega_{AMR}$

case	Ω (RPM)	R	c_{tip}	C_T/σ	ω_{adapt}	ω_{AMR}	K
UH-60A c8534	**258**	**322 in**	**22.1 in**	**.084**	**.0045**	**.009**	**0.5**
TRAM hover	**348**	**228 in**	**22.0 in**	**.142**	**.005**	**.015**	**0.33**
HART II BVI	**1041**	**2 m**	**.121 m**	**.060**	**.05**	**.122**	**0.4**

Calculating the vorticity at the core radius, $\bar{r} = 1$, along with the assumption that the core radius is proportional to the blade chord, *c*, i.e. $r_c = \beta c$

$$\omega_z(\bar{r}=1) = \frac{2\Omega R}{\pi\beta^2 c}(\frac{C_T}{\sigma})\alpha e^{-\alpha} = 0.228\frac{\Omega R}{\beta^2 c}(\frac{C_T}{\sigma}) \quad (5)$$

The key scaling is the dependence on solidity-weighted thrust coefficient, C_T/σ, and an assumption on the vortex core radius.

A typical vortex core radius is on the order of 5-10% chord [31,32] for wake ages up to 1½-2 rotor revolutions. As discussed previously, high-order CFD methods require 4-5 points to resolve a vortex core *radius*. An under-resolved physical vortex will tend to spread out to "satisfy" this numerical limitation. In doing so, however, the circulation is maintained. The grid-based vortex radius will be the minimum of the physical dimension (~0.10c) and the numerical requirement (5Δx, using the upper bound), where Δx is the off-body Cartesian grid spacing and is usually referenced to the blade chord. That is

$$\beta = \min(0.10,\ 5\Delta x/c) \quad (6)$$

To fully resolve a tip vortex of radius 10% chord requires a grid spacing of 2% chord, which is not achieved in the current calculations, due to near-body mesh limitations. A 2.5% chord off-body mesh was calculated but showed no additional improvement due to inadequate resolution in the near-body (Figure 5d). Therefore, in this work the appropriate β is 0.25, since the finest grid spacing used is 5% chord in all the AMR calculations. The estimate for the adaption threshold with a grid-based $r_c = 0.25c$ is

$$\omega_{AMR} = 3.7\frac{\Omega R}{c}(\frac{C_T}{\sigma}) \quad (7)$$

For the three configurations reported previously (UH-60A, TRAM, HART II), Table 5 compares the manually-selected adaption threshold, ω_{adapt}, to the calculated adaption threshold estimate, ω_{AMR}, (Equation 7). Recall that the vorticity value has been non-dimensionalized for the ARC3DC flow solver by a/L_{ref}, where a is the speed of sound and L_{ref} is reference length for grid non-dimensionalization, in consistent physical units. The UH-60A and TRAM grids are in inches, while the HART II grid has been non-dimensionalized by the blade chord.

A tuning factor, K, is computed in Table 5 as $\omega_{adapt}/\omega_{AMR}$. It can be included in Equation 7, and accounts for non-ideal circulation distribution, azimuthal variation in forward flight, choice of adaption location in the tip vortex for AMR, and a multitude of other approximations, both physical and numerical

$$\omega_{AMR} = 3.7K\frac{\Omega R}{c}(\frac{C_T}{\sigma}) \quad (8)$$

It is seen that for the diverse cases (high speed level flight, hover, and descending flight), the adaption parameter estimate is in good agreement with the manually chosen values for only a small range of the tuning constant (K = 0.3-0.5). Figure 7 and Figure 8 showed that the variation in computed threshold values (ω_{AMR}) produced by this range of K is within acceptable agreement with the tested values (ω_{adapt}) in order to produce meshes of reasonable feature-based resolution. Equation 8 can, therefore, serve as a good starting estimate for ω_{adapt} for AMR calculations. The exact choice of adaption threshold is not a rigorous process, but must simply not over-refine the mesh nor miss key vortical flow features. Future efforts on a wider range of rotor configurations and flight conditions will be required to further validate this a priori vorticity adaption threshold estimate.

4.2.2 Q-criterion Adaption

A widely used parameter for rotor wake visualization is the Q-criterion [33]. The Q-criterion is defined as the magnitude of the vorticity minus the magnitude of the strain

$$Q = \frac{1}{2}(\|\Omega\|^2 - \|S\|^2) \quad (9)$$

where Ω is the vorticity tensor and S is the strain rate tensor. Compared with vorticity magnitude, it has the possible advantage of ignoring shear layers, where the strain and the vorticity tend to be equal. Therefore, only vortices are identified.

A sequence of AMR grids generated using a range of *Q* values are shown in Figure 9 for the UH-60A. Indeed for high values of *Q* only the tip vortices are tagged. In the 2nd quadrant where the blade tip undergoes negative loading and the tip vortex tends to disappear, this is reflected in the grid. For lower values of *Q* the wake shear layers are increasingly captured. For *Q* values ranging from 0.1×10^{-5} to 3×10^{-5}, the AMR efficiency ranges from 0.38 to 0.18. Compared with vorticity, Q-criterion is arguably less intuitive, and its threshold value for adaption is difficult to discern, especially considering its small magnitude (order 10^{-5}). Values which are too large ($Q > 1 \times 10^{-5}$) do not results in acceptable AMR meshes, as important flow features are missed.

4.2.3 Normalized Q-criteria Adaption

To avoid the issues associated with choosing a non-intuitive dimensional-based Q-criterion adaption estimate, a normalized Q-criterion, $\overline{Q}$, has been developed [24]

$$\overline{Q} = \frac{Q}{\|S\|^2} = \frac{1}{2}\left(\frac{\|\Omega\|^2}{\|S\|^2} - 1\right) \qquad (10)$$

To counteract regions of the flow where both *Q* and *S* are small and $\overline{Q}$ becomes unreliable, a noise filter is employed using *Q* as a threshold function. The normalization removes most of the dependence on the choice of adaption threshold. Importantly, it also produces a parameter of order 1 which can be determined a priori without a flow field solution. Figure 10 shows a sequence of UH-60A AMR meshes for several reasonable values of normalized *Q* (0.1-1.0), along with the fixed refinement solution. Table 6 shows that the AMR efficiency is relatively constant (0.25-0.33). These results illustrate reduced sensitivity to the chosen threshold. While the $\overline{Q}$ = 1 result is perhaps a bit under-resolved with respect to the shear layer, this is understandable based on the definition of *Q*. Figure 11 shows the sensitivity to the noise parameter with $\overline{Q}$ = 1. For large values of the noise filter (10^{-1}) too much of the tagged region is rejected as noise. The filter effects level out for small values ($\leq 10^{-5}$), as indicated in the figure and table. Noise does not seem to be a problem in this simulation compared to other calculations which motivated this filter [24]. Since *Q* is used as the noise filter, an estimate of its dimensional value may be required. Overall, it is seen that for a realistic rotorcraft configuration normalized *Q* with noise filter provides a successful a priori AMR threshold input.

4.2.4 Adaption Frequency and Buffer Region

In addition to the adaption function and threshold, a second important input for robust application of AMR is the frequency of adaption. Adaption frequency can be changed to alter the adaption behavior, with the following constraints: For geometry-based proximity adaption, the near-body mesh outer boundary cell sizes and off-body automated refinement are designed to be commensurate. Therefore, the near-body should not move a distance which creates overlap with a less refined region of the nested Cartesian grid system. Otherwise, overset cell size compatibility becomes poor. If feature-based adaption is performed too infrequently, it is possible for the feature to leave the refined region and be dissipated or lost.

For conventional rotorcraft, the adaption frequency is driven by the rotor rotation speed and the movement of the rotor tip. For advance ratio less than 1, the tip geometry will always move farther during each time step than flow features which are convecting with the freestream. Figure 12a shows an AMR mesh at a particular time (ψ = 0 deg) and the corresponding vorticity magnitude contours for the UH-60A 0.37 advance ratio (c8534) case. Also shown are the vorticity contours 7.5 degs later (Figure 12b) on the same mesh. The maximum vorticity value shown (red) is the refinement criteria (ω_{adapt} = 0.0045). It is seen that based on the size of the adapted region, the high vorticity flow features (tip vortices) are just exiting the refined region. However, the blade geometry has moved well beyond the fine grid geometry-refinement boundaries, and is, therefore, the limiting factor setting the required frequency of adaption.

For all the unsteady configurations considered here with 5% off-body cell size, geometry and solution-based refinement are performed concurrently every 2.5 degs of rotor rotation. This means that for the UH-60A the blade tip travels 0.64 chords (almost 13 grid cells) between adaption cycles. This should be considered the upper limit of adaption frequency for geometry reasons. If the finest grid off-body spacing is reduced, the adaption frequency must also be reduced or the tag buffer region must be increased. Additional research is required to determine the effect that frequent adaption and the resulting solution interpolation has on solution accuracy and stability.

Table 6. UH-60A normalized Q-based AMR meshes

$\overline{Q}$	noise filter	AMR grid points (M)	N_{AMR}/N_{fixed}
1.0	**10^{-5}**	**37.8**	**0.25**
0.5	**10^{-5}**	**41.9**	**0.28**
0.1	**10^{-5}**	**49.5**	**0.33**
1.0	**10^{-1}**	**14.9**	**0.10**
1.0	**10^{-3}**	**30.6**	**0.20**
1.0	**10^{-5}**	**37.8**	**0.25**
1.0	**10^{-6}**	**40.9**	**0.27**
1.0	**10^{-7}**	**40.9**	**0.27**

An associated parameter is the size of the surrounding tag buffer region which is added to cells which are tagged based on geometry proximity and solution features. The tag buffer serves to expand the refinement region. The two parameters, adaption frequency and tag buffer size, are related in that they will determine together how long a feature can be tracked and when an adaption cycle is required.

Figure 13 shows the effect of the tag buffer input parameter and resulting AMR meshes for the UH-60A. As seen in Table 7 and the figure, increasing the size of the tag buffer (Figure 13c) can quickly increase the grid point count while at the same time allowing more leeway for geometry and solution features to progress in the grid without the need for frequent re-adaption. When the tag buffer is too small (Figure 13a), the grid has a somewhat jagged appearance and is not conducive to smooth movement of flow features. More frequent re-gridding is then required. In Helios, the default tag buffer is 4.

It is noted that a large tag buffer can reduce the dependency of the AMR grid on the adaption threshold value. For example, it was seen that with the normalized Q-criterion and a tag buffer of 8, the AMR grid was even less sensitive to the choice of $\overline{Q}$.

Table 7. Effect of AMR tag buffer

tag buffer (cells)	AMR grid points (M)	buffer efficiency $N/N_{baseline}$
2	**27.5**	**0.67**
4 (baseline)	**41.3**	**1.0**
6	**56.0**	**1.35**
8	**69.3**	**1.67**

4.2.5 Computational Cost

In the preceding discussions AMR was seen to offer substantial grid point savings compared with fixed refinement. The efficiencies are greatest when it is desired to track flow features a significant distance, such as in hover, BVI, or rotor-fuselage interaction. AMR is also advantageous when the general flow feature locations are not known in advance. For smaller off-body spacing than used here, the savings can be substantial. At some point uniform fixed refinement becomes infeasible. This is illustrated in Figure 14, which addresses HART II AMR calculations [34]. A physical vortex with core radius of 0.05c is shown. The current off-body grid resolution of 5% chord used here equates to 2 points across the physical vortex core, assuming the numerical scheme was capable of this feat. The figure estimates a 0.44 AMR efficiency at this resolution, which is similar to the efficiencies shown in this paper. As the number of grid points in the physical vortex is increased the fixed refinement meshes become exponentially large, while the AMR meshes increase in a much slower manner. It is estimated that to fully resolve the vortex core with the desired 8 points, fixed refinement requires 3.3 billion points, while AMR only requires 20% of that, 700 million.

The cost of an adaption is roughly on the order of 5 SAMARC steps, or one total Helios step, and is, therefore, relatively efficient given the significant re-gridding and data communication that is being performed. This typically amounts to only 1% of the total calculation cost for adaption. Compared with the cost of the near-body unstructured flow solver and the domain connectivity, the cost of AMR in Helios, at this point, is of small consequence, especially given the advantages it offers for off-body efficiencies.

5 PHYSICAL INVESTIGATIONS

To further investigate the capability of AMR, a wide range of UH-60A flight conditions have been computed using fixed refinement and unsteady AMR. Different wake refinement levels have also been simulated. Recently, a detailed summary of Helios results for the isolated UH-60A rotor with and without off-body AMR was presented [8]. These results showed that the AMR contributed to highly resolved vortex wake solutions, but had only a limited impact on airloads predictions. This is in contrast to hovering flight, where wake refinement was found to have a significant effect on the performance predictions [7,10]. Some of the comparisons with data are shown in this section, focusing on the overall impact of AMR on vortical wake resolution. Each flight condition will attempt to highlight a different aspect of the AMR calculations and data comparisons. Displaying the range of flight conditions attempts to show the generality of the AMR scheme. Previous comparisons with comparator CFD/CSD coupled simulations (i.e. fully unstructured FUN3D and structured curvilinear OVERFLOW) have shown the current simulations to be state-of-the-art [26].

The simulations use a 0.1 deg time step. Results typically employ either prescribed motions or fully coupled CFD/CSD. Adaption is performed every 2.5 deg of rotor rotations. The AMR simulations are initiated from a fixed refinement solution on a grid which is one level coarser. This 10% chord spacing fixed refinement off-body mesh contains 22 million grid points. Simulation and flow solver run parameters are detailed in the references [8,26].

5.1 High Speed (c8534)

Figure 15 shows Q-criterion iso-surfaces ($Q = 0.3\text{x}10^{-5}$) and the z = 0 grid plane for the 0.37 advance ratio c8534 conditions. Simulations have been computed on 3 fixed refinement meshes with off-body spacing of 20, 10, and 5% chord. An AMR solution is also obtained with 5% chord refinement using a vorticity criterion ($\omega_{adapt} = 0.0045$). Only every other grid point is shown for the finest refinement level (Figure 15c-d). The wake is increasingly well captured in the 3 fixed refinement results (Figure 15a-c). There is almost no distinguishable difference between the equivalently fine fixed refinement (Figure 15c) and AMR (Figure 15d) meshes, except perhaps in the 4th quadrant shear layer. The adapted grid is seen to mirror the flow features of the tip, span

break, and root vortices, and some of the shear layers – an advantage of vorticity-based refinement. The AMR wake is also much better resolved downstream, where the fixed refinement region does not extend. The AMR mesh has a 0.46 grid point efficiency (67 vs. 145 million grid points), after half a rev of adaption. Reference 2 showed that the airloads at this flight condition are not strongly influenced by the wake and show minimal differences.

A particular advantage of AMR compared with fixed refinement is the ability to track the wake far downstream without a priori knowledge and/or considerable grid point count increase. Figure 16 shows the high speed wake (vorticity contours and *Q* iso-surface) which has been convected to the downstream flow boundary. In this case the boundary was placed at 5 rotor radii from the hub center. In this case the AMR efficiency compared with a fixed refinement region which would extend to the farfield boundary is 0.33. The capability to track the wake for 5 rotor radii is remarkable.

5.2 High Thrust Coefficient (c9017)

Figure 17 shows a comparison side view of the meshes on the retreating side (62% span) along with vorticity contours for the high thrust coefficient ($C_T/\sigma = 0.126$) flight conditions. The maximum vorticity shown is the vorticity adaption refinement threshold ($\omega_{adapt} = 0.005$). Again the wake is increasingly well captured as the off-body grid is refined (Figure 17a-c). The cut off and dissipation of the wake system at the downstream boundary of the fixed refinement region is drastic. It is also seen that the fixed refinement region is poorly placed as numerous grid points are wasted above the rotor disk. The AMR solution (Figure 17d) removes the requirement to know the location of the wake a priori. The shear layers in the AMR result are not fully refined compared with the fixed refinement solutions, so that the vorticity contours differ visually. The location of the blade is indicated by the blanked out region and is seen to have geometry adaption. In this case the different levels of off-body grid refinement appeared to have some influence on the airloads distributions, as might be expected for a sensitive stalled flow condition [8].

5.3 Low Speed (c8513)

Figure 18 also shows a comparison side view of the meshes on the retreating side (62% span) along with vorticity contours for the advance ratio 0.15 low speed flight conditions (c8513). The vorticity adaption criteria is 0.0045, as in the high speed case. It is seen that the finest fixed refinement (Figure 18b) more distinctly captures some of the wake sheets and maintains the older vortices longer compared with AMR after 1 rotor revolution (Figure 18c). The older vortices (from the front of the rotor disk) are lower in the side view. The vorticity magnitude of these older structures that originated in the coarser fixed grid starting solution (Figure 18a) were not strong enough to be identified by the feature-based refinement procedure. In this sense, the fixed refinement would seem to be better capturing the wake, and the reduction in vorticity of the older vortices would appear to be an artifact of the adaption. However, additional visualization of the adapted solution after 2 rotor revolutions (Figure 18d) indicates that vortices which originate in the AMR mesh are properly maintained. This delay in adapting to the vortex is due to 1) the choice of adaption criteria and threshold, and 2) the physical time it takes for the resolved AMR regions to be ”convected” with the flow. This second point is a function of the starting conditions for the AMR calculations.

5.4 Blade-Vortex Interaction (c9812)

The UH-60A descending flight blade-vortex interaction (BVI) flight conditions are a challenging problem requiring optimal wake resolution capability in order to capture the associated high frequency loading responsible for noise generation. The UH-60A test point is investigated here using the Helios AMR capability. A full CFD/CSD coupling is performed. Previous investigations have been performed using OVERFLOW and CAMRAD II [35]. The test conditions are similar to those of HART II.

HART II has previously been simulated using Helios AMR [31]. With respect to off-body AMR, those calculations showed that in a controlled environment (i.e. the wind tunnel), it is possible to capture with exceptional accuracy the blade loadings associated with BVI. However, tuning of the vorticity-based adaption threshold is important and subject to user experience. In the above analysis (Table 5), it was shown that a reasonable estimate for the adaption threshold can be obtained a priori. Compared with fixed refinement, in some cases AMR again did not resolve the shear layers, weaker (older) vortical structures, and the vortex-shear layer interactions. Due to both near- and off-body grid resolution limitations, the current capability to model the vortex core size and strength compared with measured PIV data was woefully lacking. As reported in the reference, for the finest AMR meshes with 5% chord spacing, the computed vortex strength was 83% lower than measured values. This undoubtedly relates to the fact that the vortex core size is too large.

Figure 19a shows a z grid plane above the hub and through the Q-criterion iso-surface wake structure for the UH-60A in descending flight. AMR uniformly captures all of the vortices on the front half of the rotor disk (2^{nd} and 3^{rd} quadrants), although it misses a small region around 200 deg azimuth ($\omega_{adapt} = 0.004$). Towards the rear of the rotor disk (1^{st} and 4^{th} quadrants) the AMR grid density is more closely clustered to the tip vortices. The retreating side parallel BVIs around 315 deg azimuth appear to be well resolved and distinct in the mesh. On the advancing side, around 45 deg azimuth, the vortical features are less crisp. The Q-criterion iso-surfaces (colored by vorticity) in Figure 19b show weaker vortices in this region. These physical phenomenon and numerical investigations agree well with HART II findings, although the UH-60A flow field appears

more complicated due to the more advanced rotor planform and twist. Particularly prominent in Figure 19a is the dual system of vortices that emanate from the tip and the swept tip break (92% span).

The normal force airloads are shown in Figure 20 for the 55% and 86.5% span radial stations. The lower harmonics of normal force (Figure 20a-b) are in good agreement, but there is some variation across the front of the rotor disk, around 180 deg azimuth. This may be indicative of an error in the trim conditions or fuselage interaction effects. The 10/rev and higher harmonics in Figure 20c-d show reasonable agreement with the test data and the OVERFLOW calculations [35]. The Helios predictions tend to overestimate the BVI strengths at 55% span, although in some cases they are within the rev-to-rev data scatter (not shown). Figure 21 highlights details of the advancing and retreating side higher harmonic BVI airloads at 86.5% span. While the strongest peaks are exceptionally well captured, there appears to be significant overprediction on many of the other pulses and a minor phase error. Due to increased wake fidelity, the Helios results are an improvement over the OVERFLOW calculations, which use only 10% chord spacing, whereas the Helios AMR results use 5% chord spacing. The agreement with data is also better compared to coarser Helios off-body meshes.

5.5 Rotor-Fuselage Interaction (c8515)

The ability to track wake vortices over long distances, as illustrated in Figure 16, holds considerable promise for interactional aerodynamics. With this in mind, a low speed 0.11 advance ratio rotor-fuselage configuration is considered. CSD motions have been obtained from a rotor-alone simulation using Helios.

Vorticity contours at two spanwise locations are studied. Figure 22a shows a cut through a streamwise plane at the mid-span of the UH-60A horizontal tail in the vicinity of the tail rotor (not shown) on the advancing side. On any generic helicopter configuration, this could easily be the location of the tail rotor, or H- or T-tail. The possibility of adverse interactions of the main rotor wake with the empennage, resulting in vibration, poor handling qualities, or anti-torque deficiencies, is evident. Such interferences have plagued numerous helicopter development programs over the years, with hardly a single rotorcraft program that has not resulted in a tail redesign during initial development (e.g. Black Hawk, Apache, V-22 Osprey, Comanche). Separation on the undeflected horizontal lower surface in seen in the figure (normally the horizontal tail on the UH-60A would be deflected for these flight conditions). Figure 22b is a cut at 50% rotor radius on the advancing side. One might consider a wing, propulsor, or weapons system at this location in line with the rotor hub on a future compound or high speed rotorcraft configuration. The ability of AMR to capture the vortices as they descend below the fuselage holds promise for predicting new and unanticipated adverse rotor-fuselage interactions earlier in the design process.

A visualization of the rotor wake using the Q-criterion in Figure 23a-b shows that the upper part of the vertical tail (i.e. the UH-60A tail rotor location) interacts with the main rotor tip vortices. In Figure 23b the wake in the off-body grids is colored blue, while the near-body wake is green. The grids in this region are shown in Figure 23c. It is clear that as the tip vortices convect into the near-body grid, they are completely dissipated. This unfortunate circumstance is the result of the coarse near-body grid, 2^{nd}-order formulation of the unstructured CFD solver, and spacing mismatch between overset Cartesian and unstructured cells. The unstructured mesh was not refined in the grid generation phase for this kind of calculation. The off-body AMR continues to capture the downstream vortices nonetheless.

In the wake visualizations the closely-coupled paired vortices in the tail rotor region (Figure 22) appear to originate from the blade tip and the span break. Although the axial twisting of these vortices (Figure 23b) around each on either side would assume to be physical, the numerical artifacts due to the near-body void and the disconnected filaments are unknown.

A drawback of complex configuration AMR is the excessive number of grids that can be generated; 10736 in this case after 3.5 rotor revolutions. This puts a strain on the domain connectivity and visualization modules.

6 CONCLUSIONS

The modular, multidisciplinary Helios flow simulation software has been used to study the effects of rotorcraft wake resolution and refinement. Numerous simulations using adaptive mesh refinement (AMR) on a range of configurations across the operating envelope (hover, high speed, low speed, high C_T, BVI, rotor-fuselage interaction) have been investigated in order to draw the following conclusions regarding AMR for helicopter simulations:

- A combination of both near- and off-body mesh refinement is necessary for accurate rotorcraft flow field simulations.
- An a priori estimate of the adaption threshold is required for convenient and robust use of AMR in a production environment. A vorticity value scaled to physical rotor parameters or a normalized Q-criterion is shown to provide an excellent starting point.
- Compared with fixed refinement, AMR with a vorticity or Q-criterion-based refinement parameter misses some of the shear layers and older vortices, which have lower associated threshold values.
- AMR adaption frequency and tag buffer size must be considered based on flow conditions, geometry motion, grid point count, and cost. For advance ratio less than one, geometry-based adaption frequency is the limiting factor.
- In cases tested here which do not have fully resolved vortices, AMR provides a 50-80% reduction in grid point count compared with fixed refinement.

- Increasing refinement in the off-body wake region results in significantly improved wake vortex capturing. AMR has the particular advantage of being able to maintain and convect the wake for long distances; 5 rotor radii is demonstrated. This facilitates clearer understanding of rotor-fuselage-empennage-tail rotor interactions.
- Improvement in airloads prediction is not always commensurate with increased off-body refinement. BVI airloads are seen to be the most sensitive to accurate wake resolution.
- In order to be fully effective AMR meshes must be allowed to "convect" and develop with the flow in order to resolve downstream flow features.

7 ACKNOWLEDGEMENTS

Material presented in this paper is a product of the CREATE-AV element of the Computational Research and Engineering for Acquisition Tools and Environments (CREATE) Program sponsored by the U.S. Department of Defense High Performance Computing (HPC) Modernization Program Office. This work was conducted at the HPC Institute for Advanced Rotorcraft Modeling and Simulation (HIARMS). The authors are grateful for the significant computational resources provided by the HPC DoD Supercomputing Resource Centers. The NASA Langley GEOLAB provided the unstructured UH-60A fuselage mesh. Helpful discussions with Drs. Venke Sankaran, Joon Lim, and Mr. Arsenio Dimanlig are appreciated.

8 REFERENCES

1. Strawn, R.C., and Barth, T. J., "A Finite-Volume Euler Solver for Computing Rotary-Wing Aerodynamics on Unstructured Meshes," *Journal of the American Helicopter Society*, Vol. 38, 1993, pp.61–67.
2. Kang, H. J., and Kwon, O. J., "Effect of Wake Adaptation on Rotor Hover Simulations Using Unstructured Meshes," *Journal of Aircraft*, Vol. 38, No. 5, Sept.-Oct. 2001, pp. 868-877.
3. Yu, D. O., and Kwon, O. J., "Viscous Flow Simulation of the HART II Rotor Using Unstructured Adaptive Meshes," 36th European Rotorcraft Forum, Paris, France, September 2010.
4. Shenoy, R., and Smith, M. J., "Unstructured Overset Grid Adaption for Rotorcraft Aerodynamic Interactions," American Helicopter Society 67th Annual Forum, Virginia Beach, VA, May 2011.
5. Dietz, M., Kramer, E., and Wagner, S., "Tip Vortex Conservation on a Main Rotor in Slow Descent Flight Using Vortex-Adapted Chimera Grids," AIAA-2006-3478, 24th AIAA Applied Aerodynamics Conference, San Francisco, CA, June 2006.
6. Meakin, R. L., "Automatic Off-body Grid Generation for Domains of Arbitrary Size," AIAA-2001-2536, 15th AIAA Computational Fluid Dynamics Conference, Anaheim CA, June 2001.
7. Wissink, A., Potsdam, M., Sankaran, V., Sitaraman, J., Yang, Z., and Mavriplis, D., "A Coupled-Unstructured Adaptive Cartesian CFD Approach for Hover Prediction," American Helicopter Society 66th Annual Forum, Phoenix, AZ, May 2010.
8. Sitaraman, J., Potsdam, M., Jayaraman, B., Datta, A., Wissink, A., Mavriplis, D., and Saberi, H., "Rotor loads Prediction Using Helios: A Multi-Solver Framework for Rotorcraft CFD/CSD Analysis," AIAA-2011-1230, AIAA 49th Aerospace Sciences Meeting, Orlando, FL, January 2011.
9. Buning, P. G., and Pulliam, T. H., "Cartesian Off-Body Grid Adaption for Viscous Time-Accurate Flow Simulations," AIAA-2011-3693 20th AIAA Computational Fluid Dynamics Conference, Honolulu, HI, June 2011.
10. Chaderjian, N., and Buning, P., "High Resolution Navier-Stokes Simulation of Rotor Wakes," American Helicopter Society 67th Annual Forum, Virginia Beach, VA, May 2011.
11. Nielsen, E., Lee-Rausch, E., and Jones, W., "Adjoint-Based Design of Rotors in a Noninertial Reference Frame," *Journal of Aircraft*, vol. 47, No. 2, 2010, pp. 638-646.
12. Sankaran, V., US Army AMRDEC, Private communication, 2009.
13. Hariharan, N., and Sankar, L., "High-Order Essentially Non-oscillatory Schemes for Rotary-Wing Wake Computations," *Journal of Aircraft*, Vol. 41, No. 2, 2004, pp. 258–267.
14. Yeshala, N., A.T. Egolf, R. Vasilescu, and L. Sankar, "Application of Higher Order Spatially Accurate Schemes to Rotors in Hover," AIAA Paper 2006-2818, 24th AIAA Applied Aerodynamics Conference, San Francisco, CA, June 2006.
15. Nastase, C., Mavriplis, D., and Sitaraman, J., "An Overset Unstructured Mesh Discontinuous Galerkin Approach for Aerodynamic Problems," AIAA Paper 2011-0195; 49th AIAA Aerospace Sciences Meeting and Exhibit, Orlando FL, January 2011.
16. Chen, C., Chen, Y., Chen, B., Jain, R., Wang, Z. J., and Lund, T., "High Fidelity Multidisciplinary Tool Development For Helicopter Quieting," AIAA 2007-3807, 25th AIAA Applied Aerodynamics Conference, San Francisco, CA, June 2007.
17. Wissink, A., Sitaraman, J., Mavriplis, D., Pulliam, T., and Sankaran, V., "A Python-based Infrastructure for Overset CFD with Adaptive Cartesian Grids," AIAA-2008-0927, AIAA 48th Aerospace Sciences Meeting, Reno, NV, January 2008.
18. Mavriplis, D., "Adaptive Meshing Techniques for Viscous Flow Calculations on Mixed Element Unstructured Meshes," *International Journal for Numerical Methods in Fluids*, Vol. 34, No.2, September 2000, pp. 93-111.
19. Wissink, A., Kamkar, S., Pulliam, T., Sitaraman, J., and Sankaran, V., "Cartesian Adaptive Mesh Refinement for Rotorcraft Wake Resolution," AIAA-2010-4554, AIAA 28th Applied Aerodynamics Conference, Chicago, IL, June 2010.

20. Hornung, R. D., Wissink, A. M., and Kohn, S. R., "Managing Complex Data and Geometry in Parallel Structured AMR Applications," *Engineering with Computers*, Vol. 22, No. 3-4, Dec. 2006, pp. 181-195. Also see www.llnl.gov/casc/samrai.
21. Pulliam, T. H., "High Order Accurate Finite-Difference Methods: as seen in OVERFLOW," AIAA-2011-3851, 20th AIAA Computational Fluid Dynamics Conference, Honolulu, HI, June 2011.
22. Sitaraman, J., Floros, M., Wissink, A., and Potsdam, M., "Parallel Domain Connectivity Algorithm For Unsteady Flow Computations Using Overlapping And Adaptive Grids," *Journal of Computational Physics*, Volume 229, Issue 12, p. 4703-4723.
23. Berger, M.J., and Oliger, J., "Adaptive Mesh Refinement for Hyperbolic Partial Differential Equations," *Journal of Computational Physics*, Vol. 53, 1984, pp. 484–512.
24. Kamkar, S., Jameson, A., Wissink, A., and Sankaran, V., "Automated Off-Body Cartesian Mesh Adaption for Rotorcraft Simulations," AIAA-2011-1269, AIAA 49th Aerospace Sciences Meeting, Orlando, FL, January 2011.
25. Kufeld, R., Balough, D., Cross, J., Studebaker, K., Jennison, C., and Bousman, W., "Flight Testing of the UH-60A Airloads Aircraft," American Helicopter Society 50th Annual Forum, Washington, DC, May 1994.
26. Sankaran, V., Potsdam, M., Wissink, A., Datta, A., Jayaraman, B., and Sitaraman, J., "Rotor Loads Prediction in Level and Maneuvering Flight Using Unstructured-Adaptive Cartesian CFD," AHS 67th Annual Forum, Virginia Beach, VA, May 2011.
27. Lim, J., Nygaard, T., Strawn, R., and Potsdam, M., "BVI Airloads Prediction Using CFD/CSD Loose Coupling," *Journal of the American Helicopter Society*, Vol. 52, No. 4, October 2007, pp. 43-58.
28. Young, L. A., Booth Jr., E. R., Yamauchi, G. K., Botha, G., and Dawson, S., "Overview of the Testing of a Small-Scale Proprotor," American Helicopter Society 55th Annual Forum, Montreal, Canada, May 1999.
29. Mavriplis, D. J., Unstructured Mesh Discretizations and Solvers for Computational Aerodynamics, *AIAA Journal*, Vol. 46, No. 6, pp. 1281 - 1298, June 2008.
30. Potsdam, M., and Mavriplis, D., "Unstructured Mesh CFD Aerodynamic Analysis of the NREL Phase VI Rotor," 47th AIAA Aerospace Sciences Meeting, AIAA Paper 2009-1221, Orlando, FL, January 2009.
31. Lim, J., Wissink, A., Jayaraman, B., and Dimanlig, A., "Application of Adaptive Mesh Refinement Technique in Helios to Blade-Vortex Interaction Loading and Rotor Wakes," American Helicopter Society 67th Annual Forum, Virginia Beach, VA, May 2011.
32. Leishman, J. G., Principles of Helicopter Aerodynamics, New York: Cambridge University Press, 2006.
33. Jeong, J., and Hussain, F., "On the Identification of a Vortex," *Journal of Fluid Mechanics*, Vol. 285, 1985, pp. 69-94.
34. Jayaraman, B., Wissink A., Lim, J., Dimanlig, A., and Potsdam, M., "Blade-Vortex Interaction and Rotor Wake Prediction using the Helios Flow Solver," HPC User's Group Meeting, Portland, OR, June 2011.
35. Lim, J., "An Assessment of Rotor Dynamics Correlation for Descending Flight Using CFD/CSD Coupled Analysis," American Helicopter Society 64th Annual Forum, Montreal, Canada, May 2008.

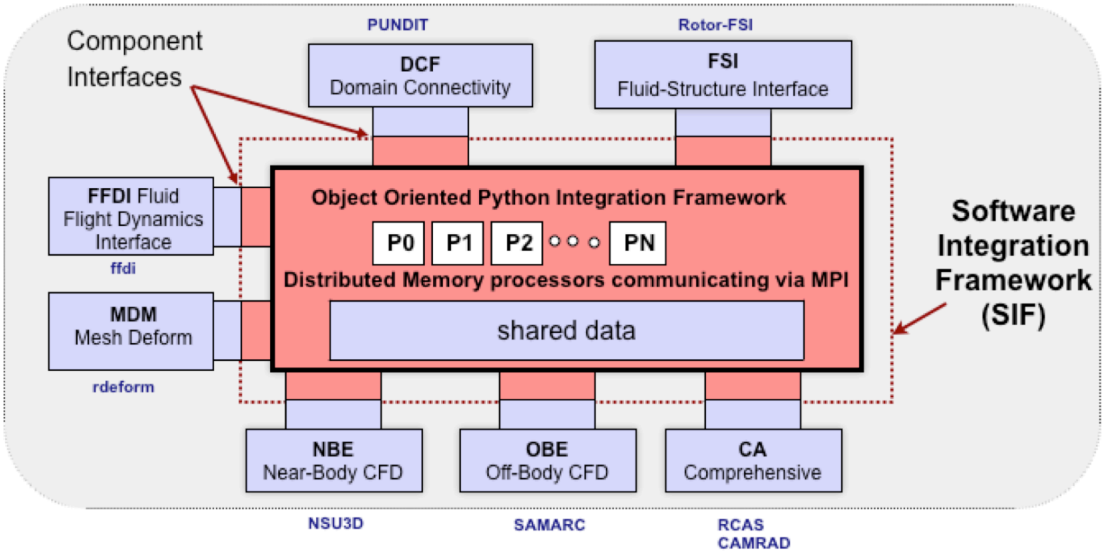

Figure 1. Schematic representation of the Helios Software Integration Framework (SIF)

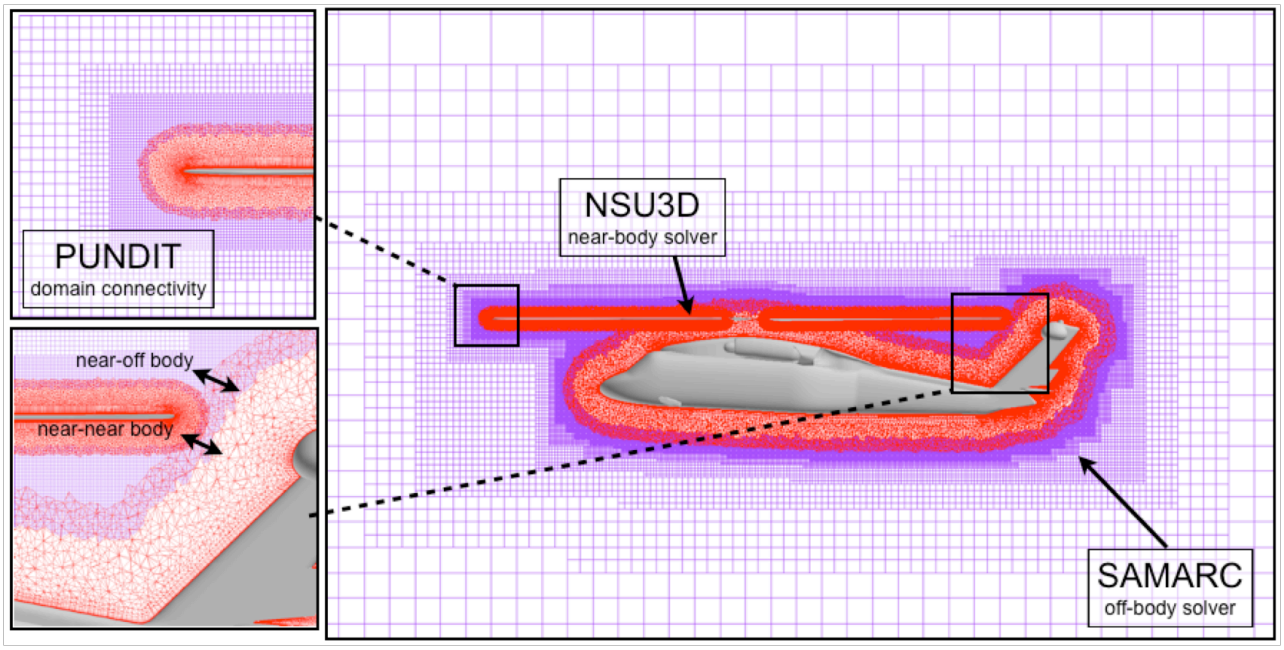

Figure 2. Helios dual-mesh overset CFD approach

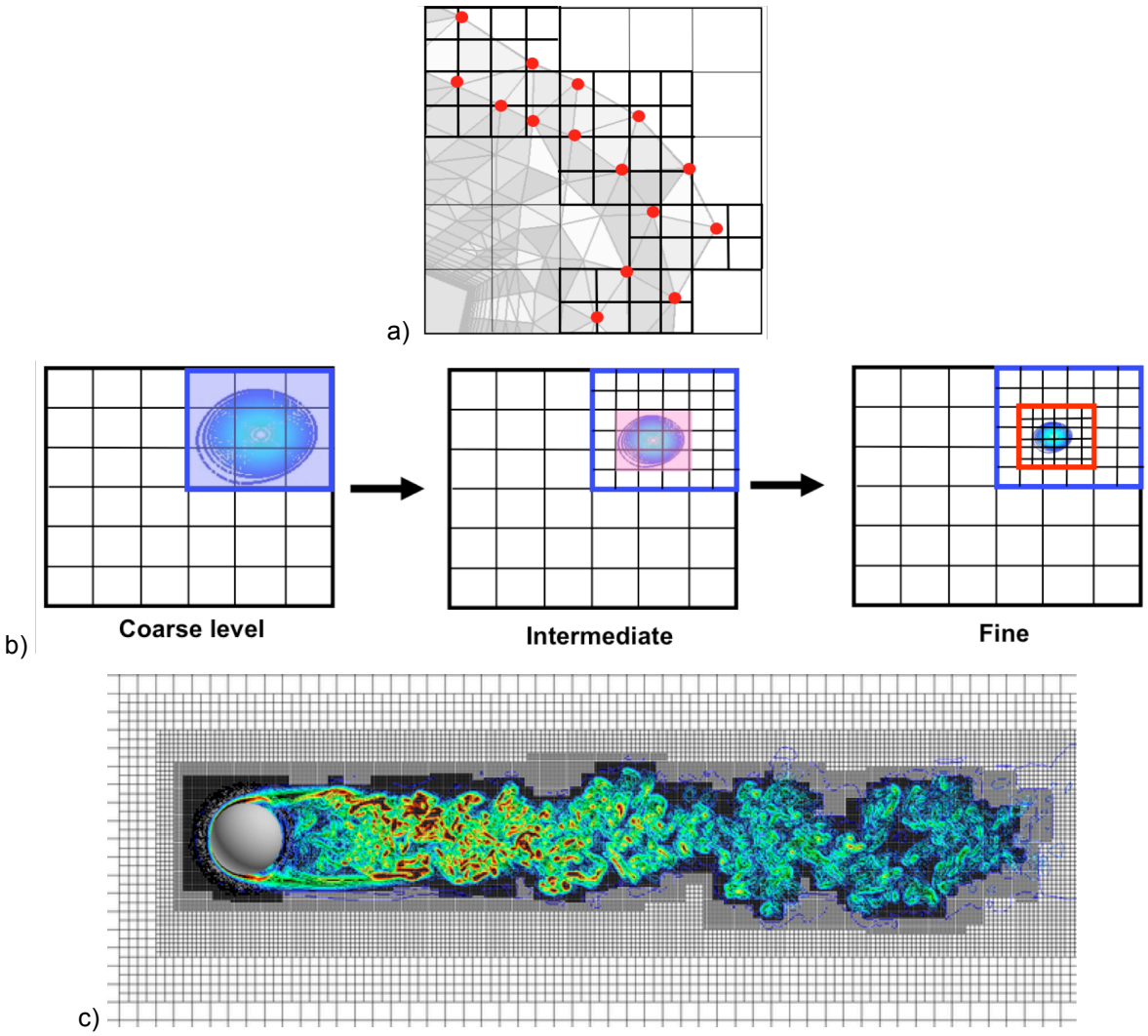

Figure 3. Off-body adaptive mesh refinement: a) geometry-based procedure , b) feature-based procedure, c) feature-based example

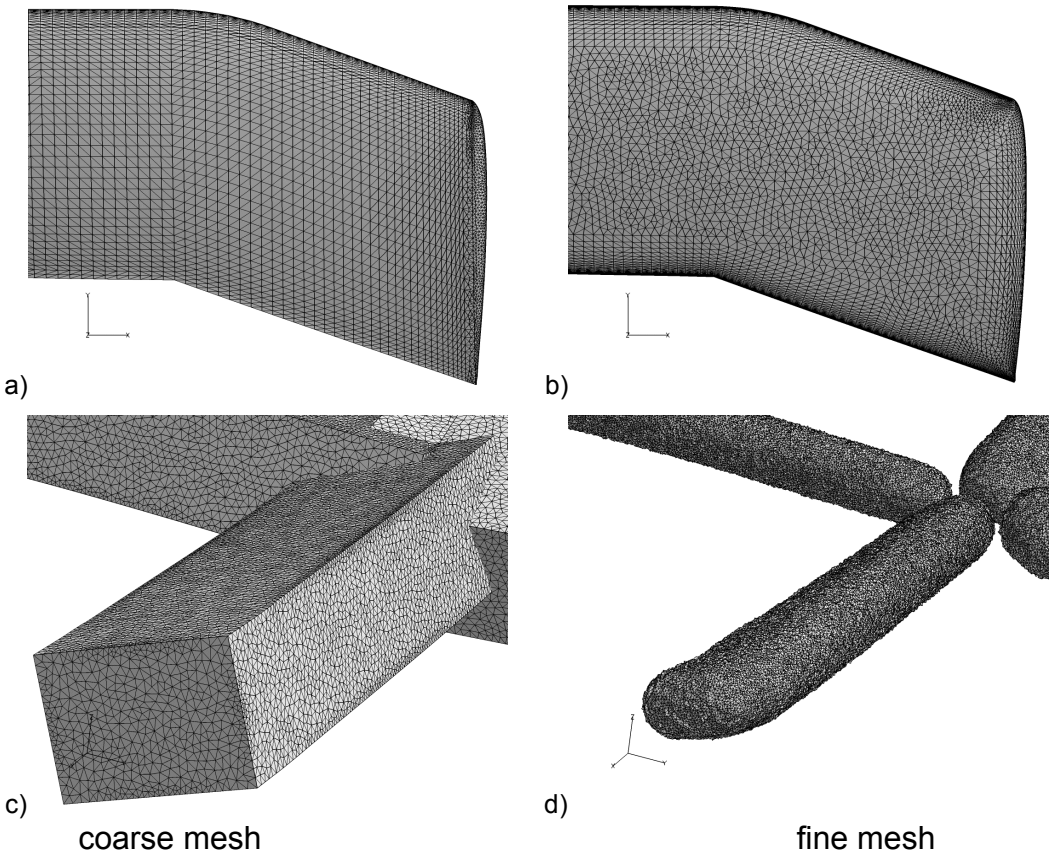

Figure 4. UH-60A unstructured near-body meshes: a-b) surface mesh, c-d) outer boundary

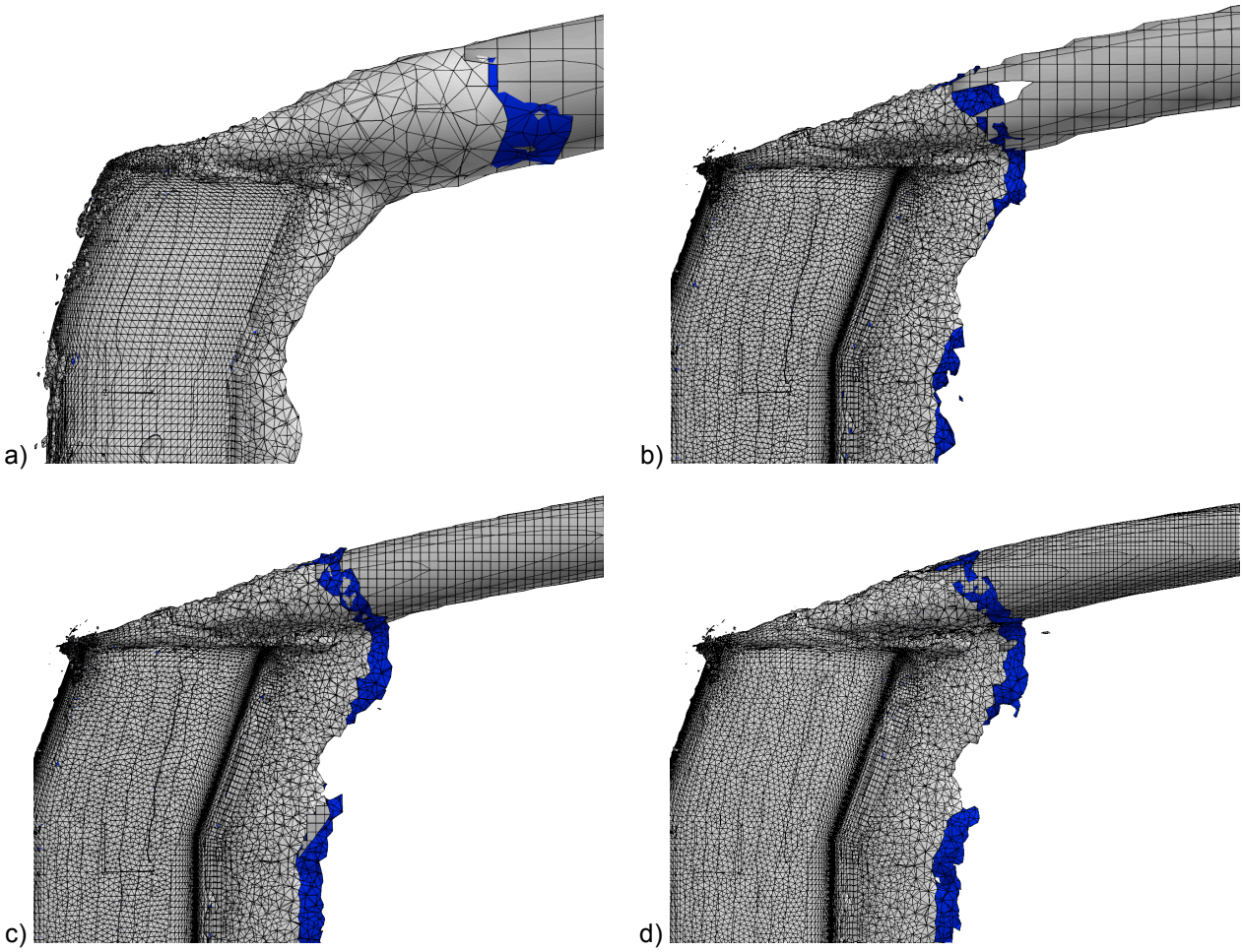

Figure 5. UH-60A blade tip and tip vortex vorticity iso-surface: a) coarse near-body (NB), 20% chord off-body (OB) spacing, b) fine NB, 10% chord OB, c) fine NB, 5% chord OB, d) fine NB, 2.5% chord OB. Blue is NB overlap region.

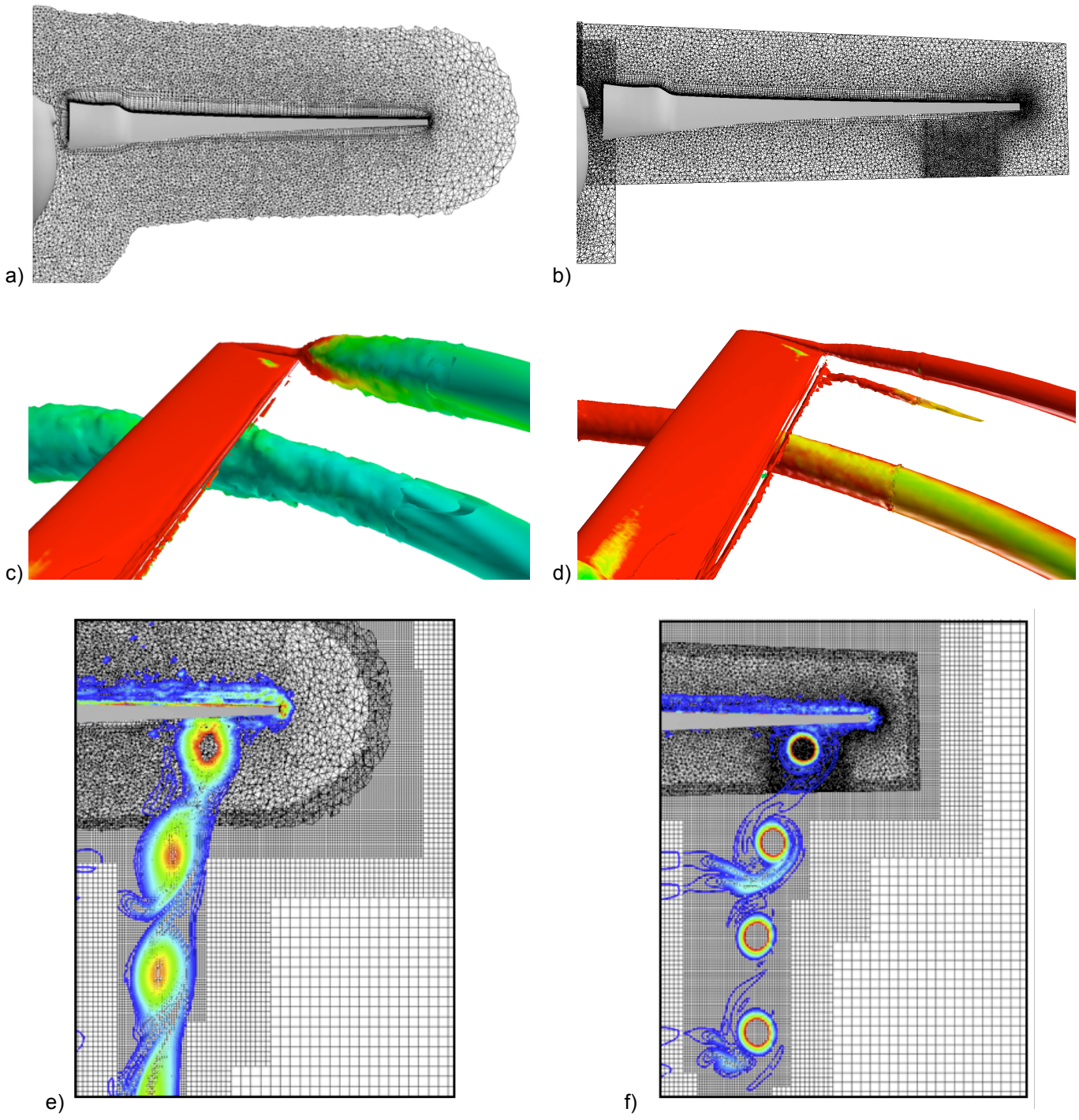

Figure 6. TRAM rotor in hover: a-b) volume mesh, c-d) Q-criterion iso-surface of tip vortex and first blade passing colored by vorticity, e-f) wake vorticity contours

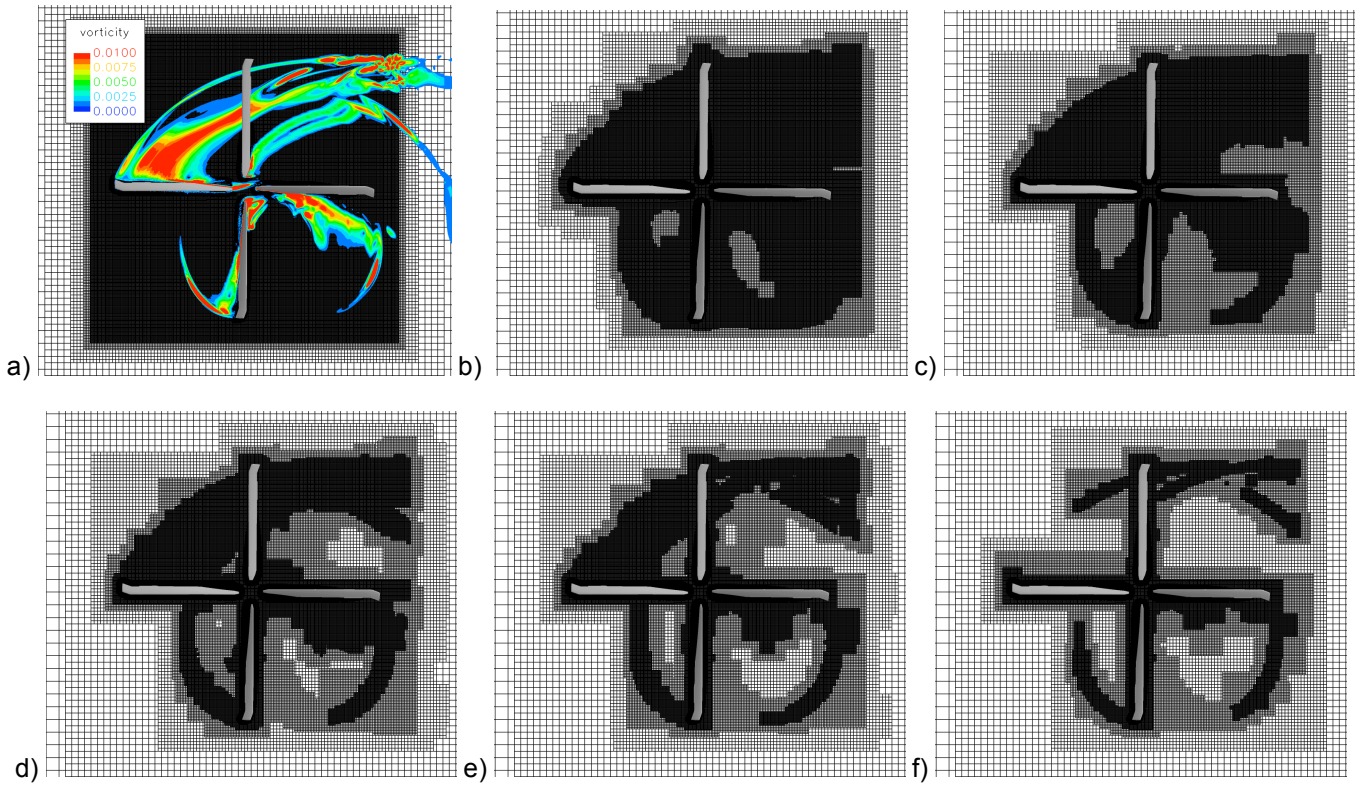

Figure 7. UH-60A forward flight vorticity-based AMR z = 0 plane: a) fixed refinement with vorticity contours, b) ω_{adapt} = 0.00045, c) ω_{adapt} = 0.0025, d) ω_{adapt} = 0.0045, e) ω_{adapt} = 0.0065, f) ω_{adapt} = 0.0135

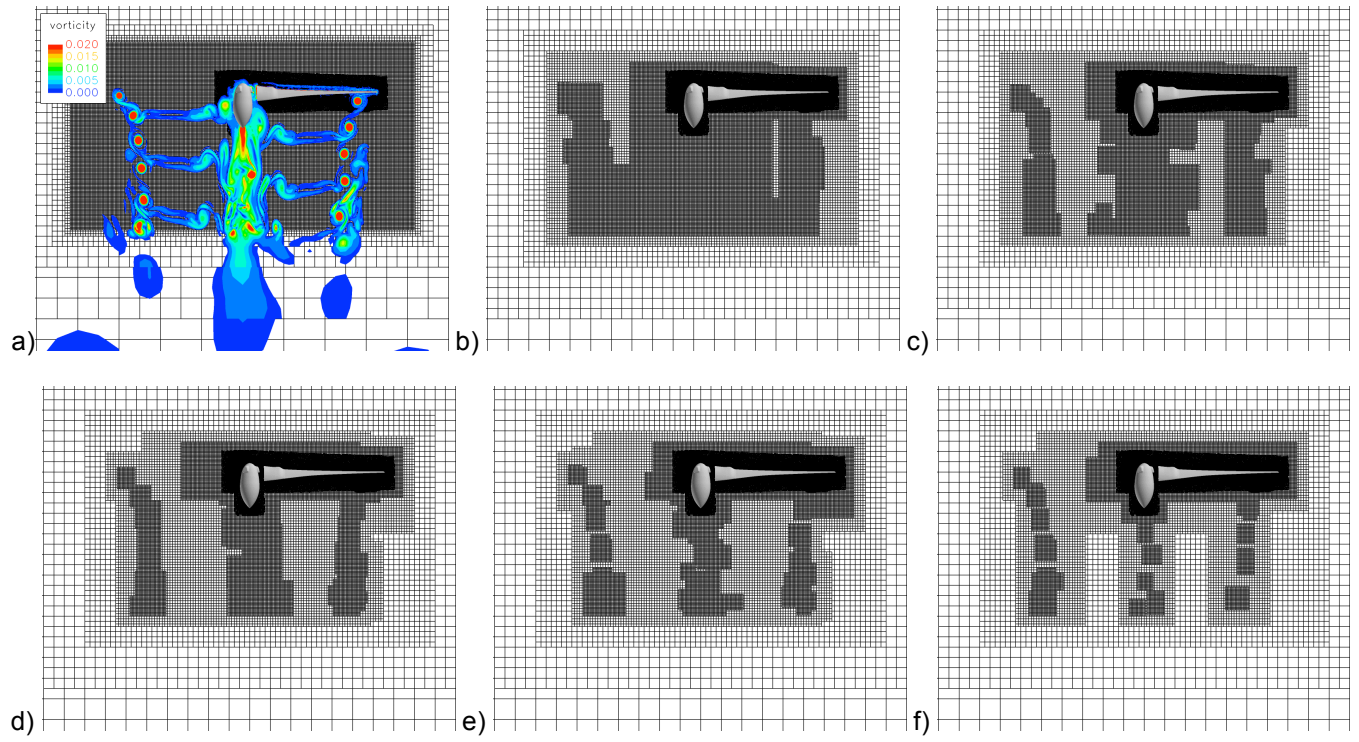

Figure 8. TRAM hover vorticity-based AMR y = 0 plane: a) fixed refinement with vorticity contours, b) ω_{adapt} = 0.0025, c) ω_{adapt} = 0.0050, d) ω_{adapt} = 0.0075, e) ω_{adapt} = 0.0100, f) ω_{adapt} = 0.0150

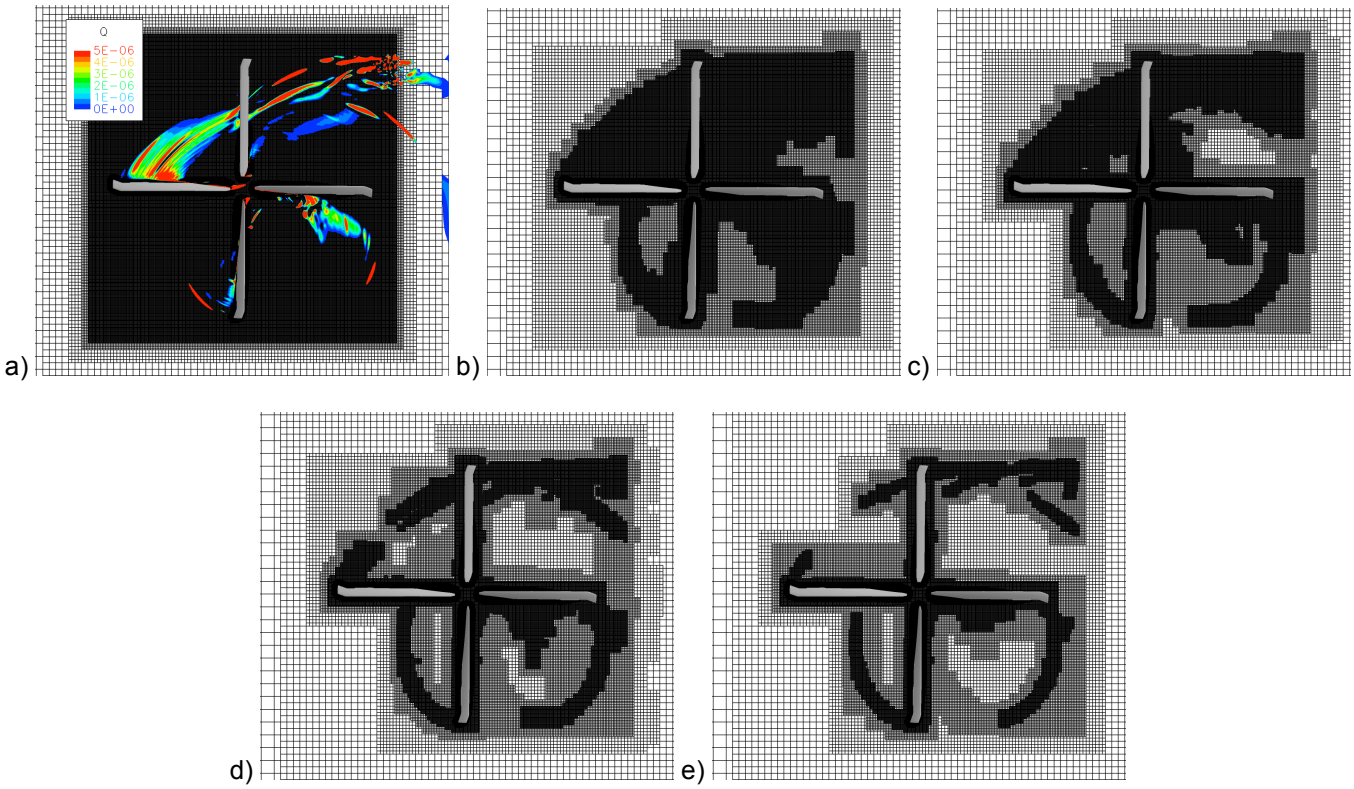

Figure 9. UH-60A forward flight Q-based AMR z = 0 plane: a) fixed refinement with Q contours, b) Q = 0.1x10^{-5}, c) Q = 0.3x10^{-5}, d) Q = 1x10^{-5}, e) Q = 3x10^{-5}

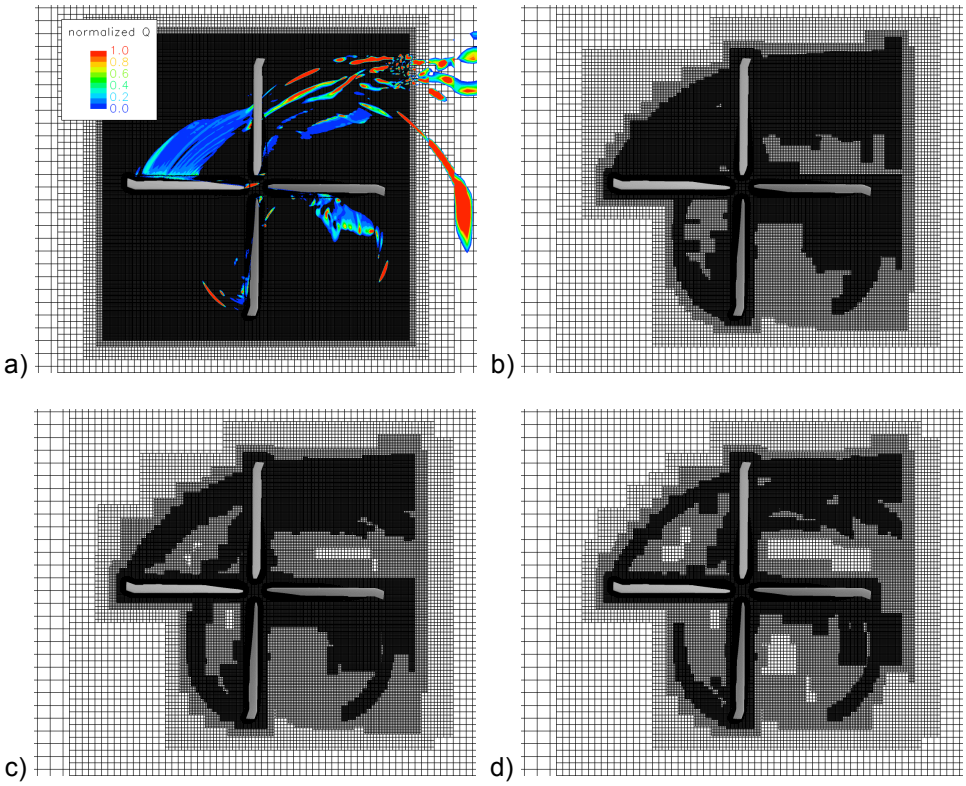

Figure 10. UH-60A forward flight normalized Q-based AMR z = 0 plane: a) fixed refinement with normalized Q contours, b) $\overline{Q}$ = 0.1, c) $\overline{Q}$ = 0.5, d) $\overline{Q}$ = 1.0, noise filter = 10^{-5}

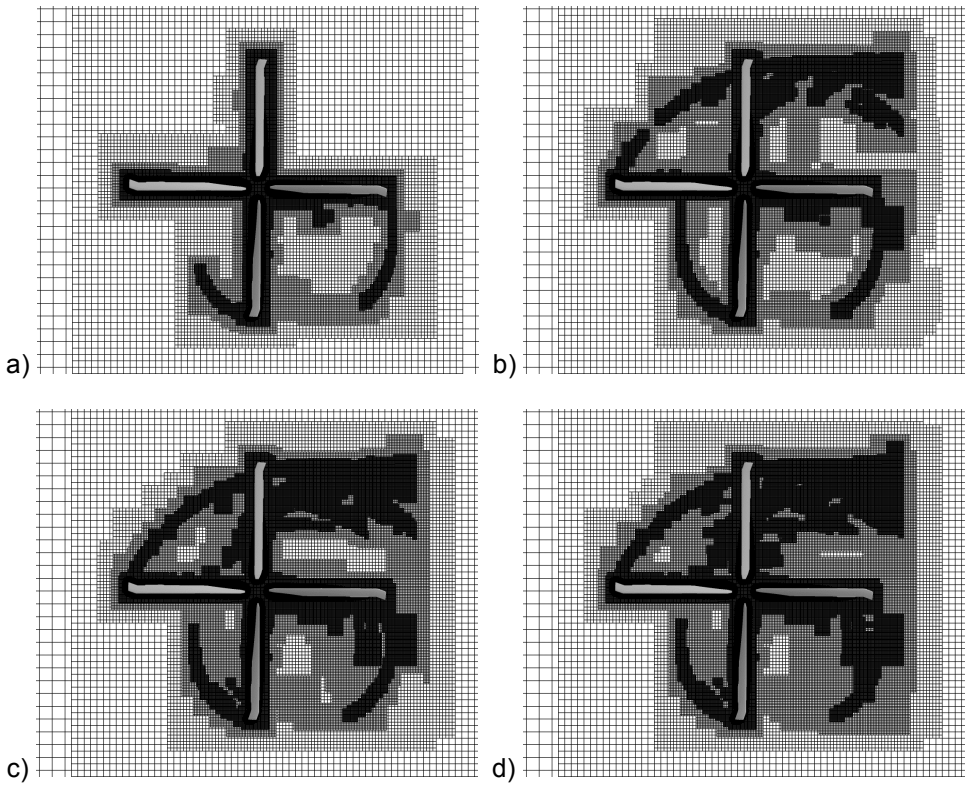

Figure 11. UH-60A forward flight normalized Q-based AMR z = 0 plane: noise filter = a) 10^{-1}, b) 10^{-3}, c) 10^{-5}, d) 10^{-7}, $\overline{Q}$ = 1

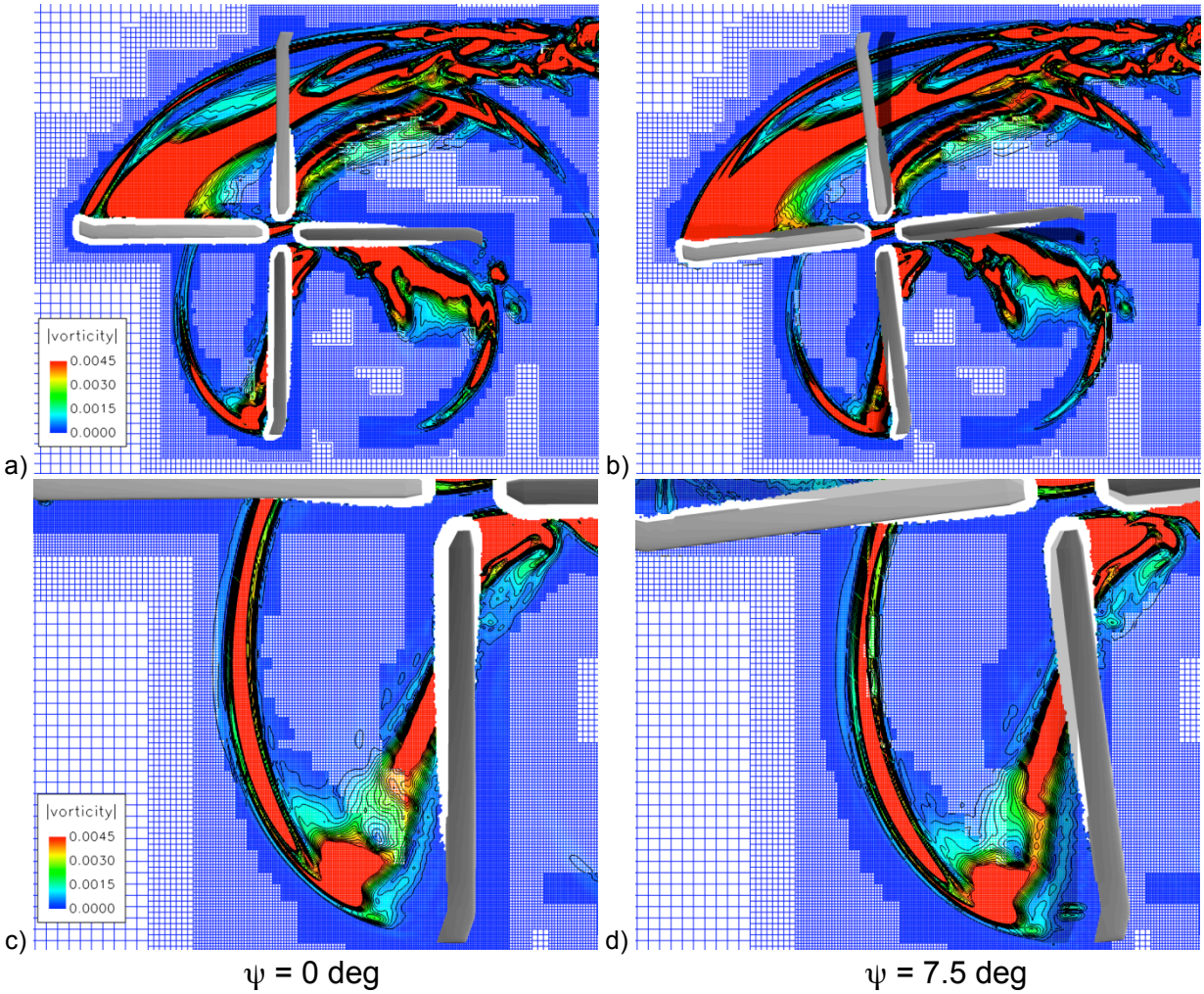

Figure 12. Effect of adaption frequency for high speed wake a) AMR mesh and vorticity magnitude at ψ = 0 deg b) solution at ψ = 7.5 deg on same AMR mesh, c-d) blow up of third-quadrant tip vortex and blade tip

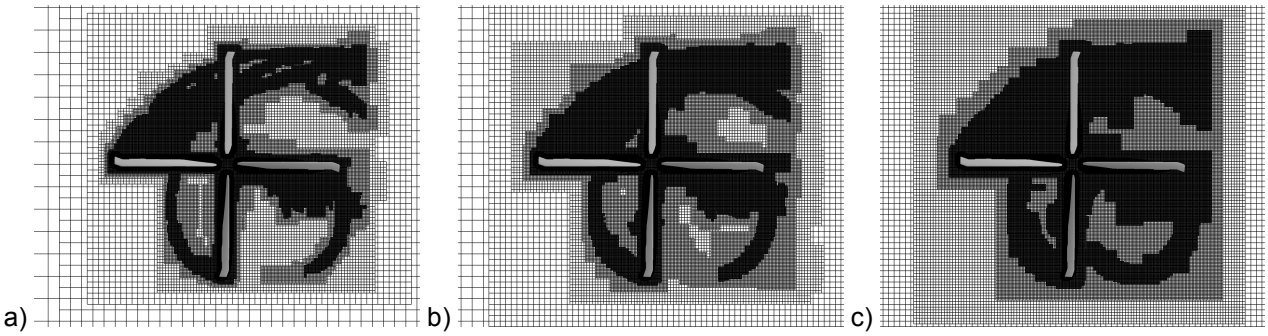

Figure 13. Effect of tag buffer size: tag buffer = a) 2, b) 4, c) 8 cells, ω_{adapt} = 0.0045

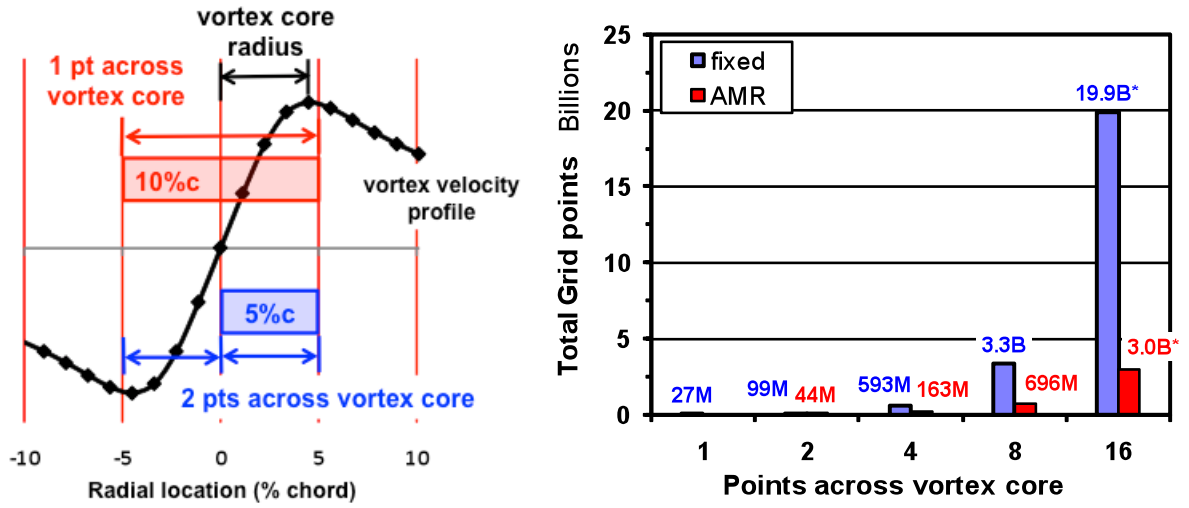

Figure 14. Discrete numerical resolution of physical vortex (r_c = 0.05c): a) vortex velocity profile, b) grid size estimate – fixed refinement compared with AMR [34]

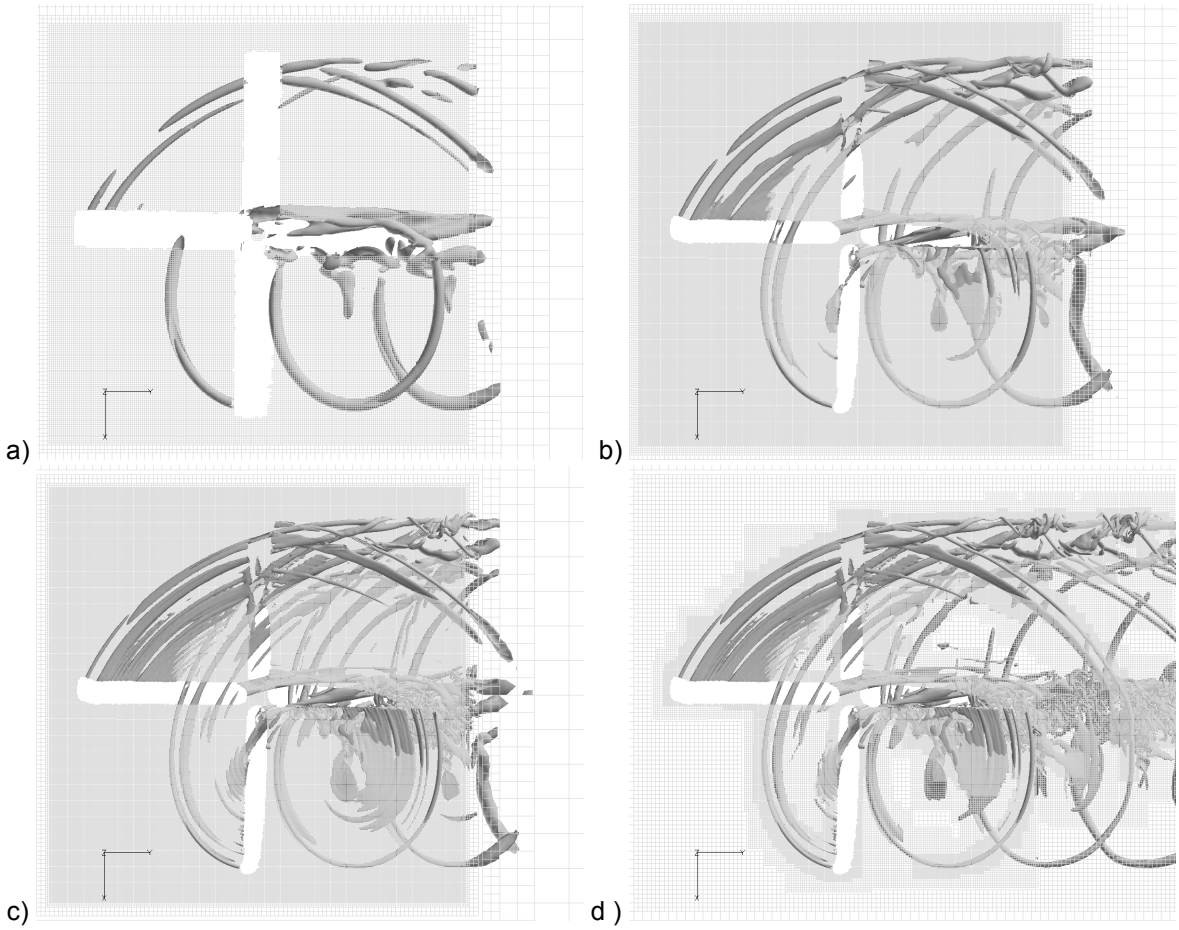

Figure 15. UH-60A high speed (c8534) wakes, Q-criterion iso-surfaces, z = 0 grid plane: a) fixed refinement – 20% chord, b) fixed refinement – 10% chord, c) fixed refinement – 5% chord, d) AMR – 5% chord

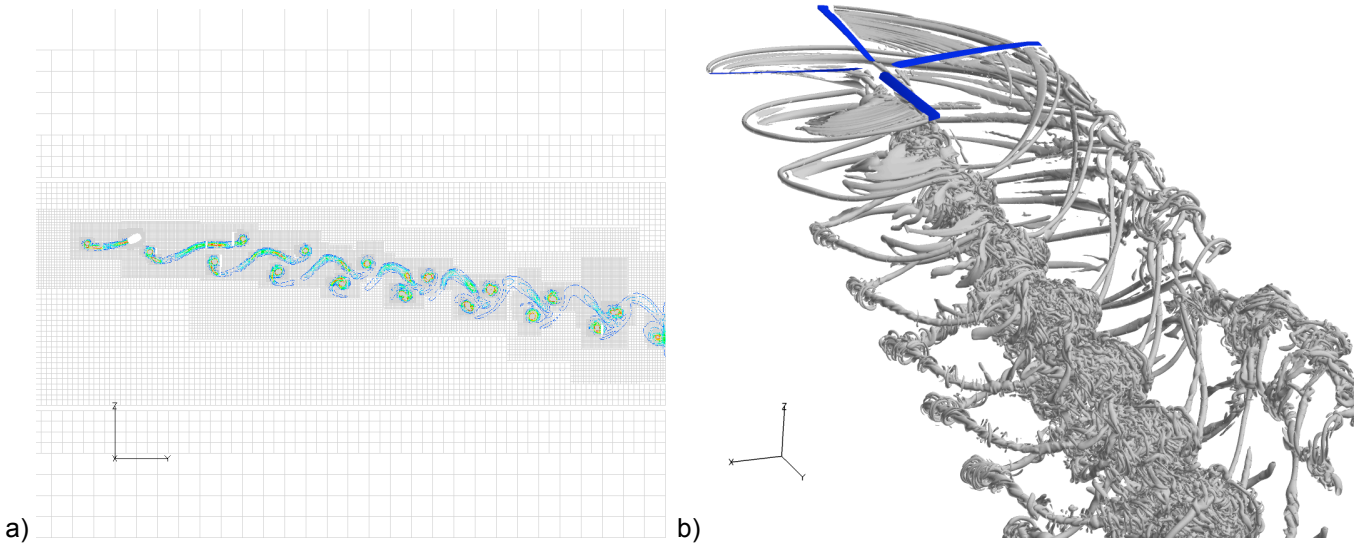

Figure 16. UH-60A high speed (c8534) wake tracking to CFD outer boundary: a) vorticity contours, r/R = 62% span (retreating side), b) Q-criterion iso-surface

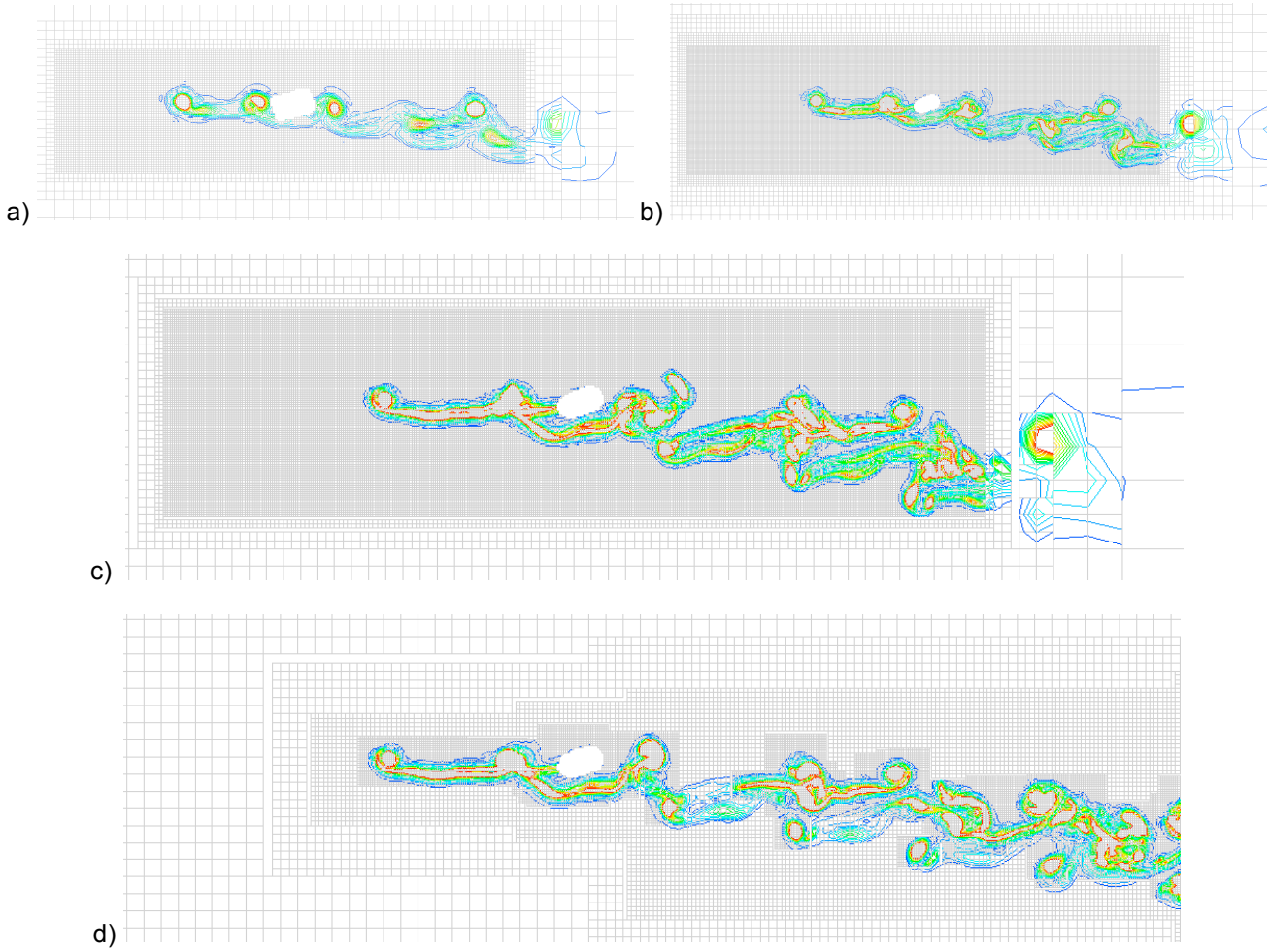

Figure 17. UH-60A high thrust coefficient (c9017) wake comparisons, vorticity contours, r/R = 62% span (retreating side) grid plane: a) fixed refinement – 20% chord, b) fixed refinement – 10% chord, c) fixed refinement – 5% chord, d) AMR after 2 revolutions – 5% chord

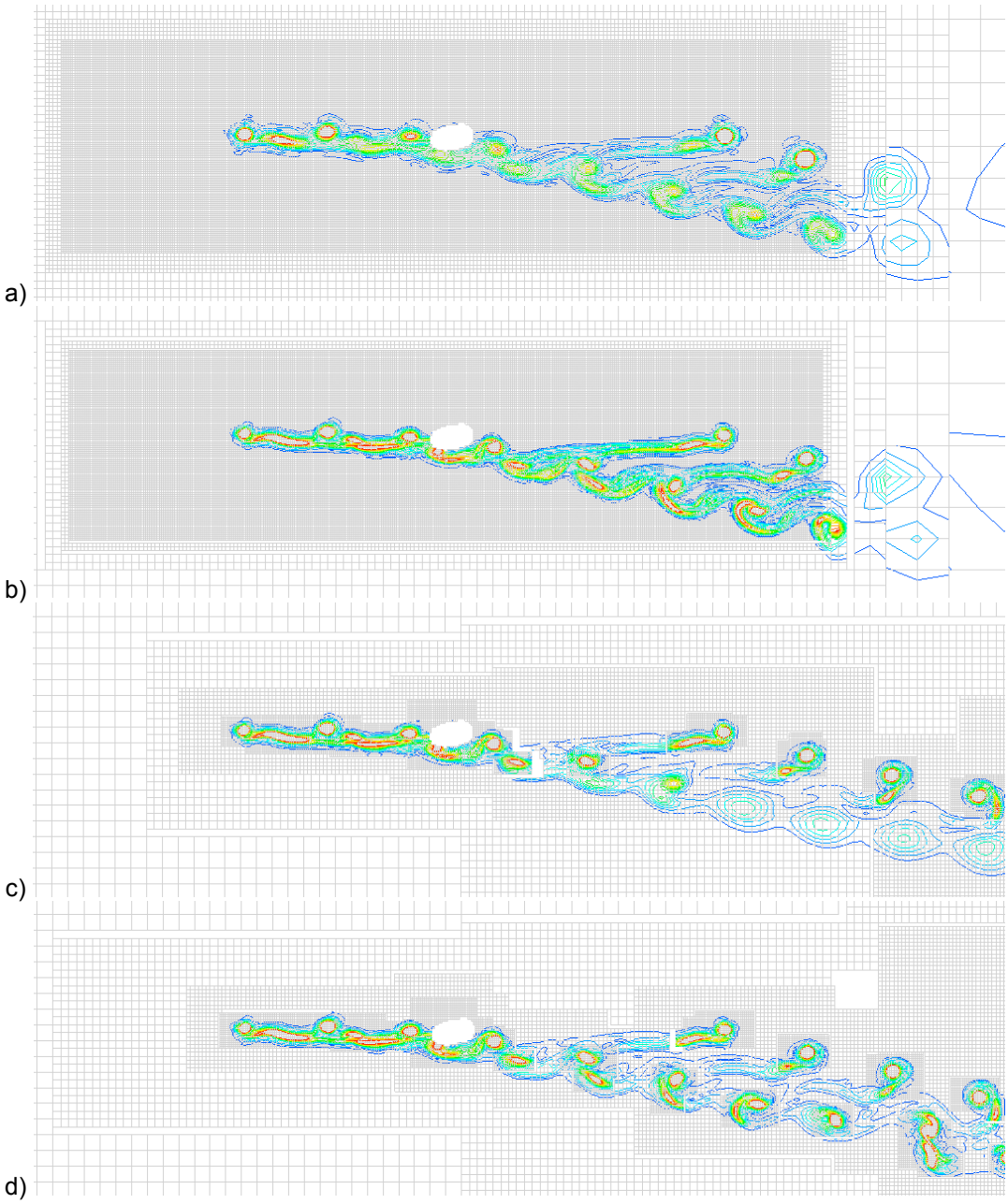

Figure 18. UH-60A low speed (c8513) wake comparisons, vorticity iso-surfaces, r/R = 62% span (retreating side) grid plane: a) fixed refinement – 10% chord, b) fixed refinement – 5% chord, c) AMR after 1 revolution – 5% chord, d) AMR after 2 revolutions – 5% chord. (Extraneous Cartesian holes are visualization artifacts)

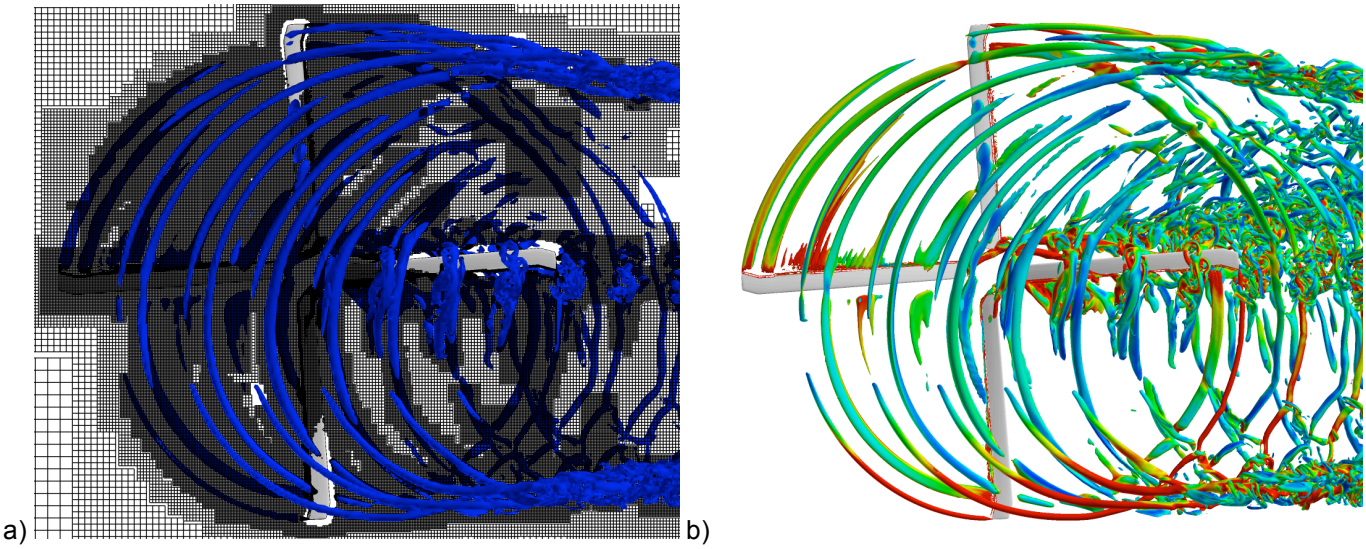

Figure 19. UH-60A descending flight blade-vortex interaction (c9812) wake Q-criterion iso-surfaces: a) z grid plane through BVI, b) colored by vorticity

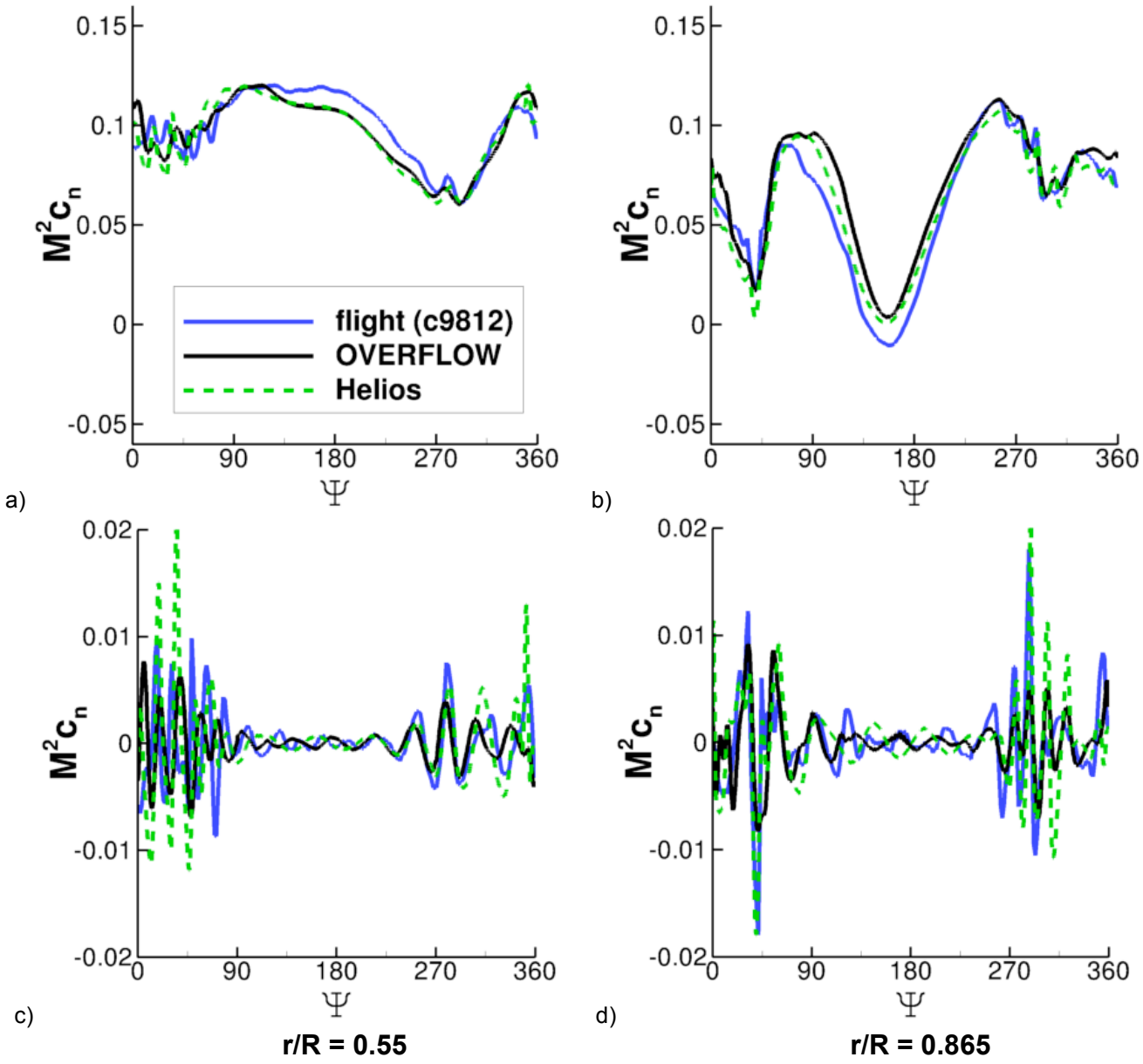

Figure 20. UH-60A descending flight blade-vortex interaction (c9812) normal force airloads at r/R = 0.55 and 0.865: a-b) normal force coefficient, c-d) higher harmonics of normal force (10+/rev)

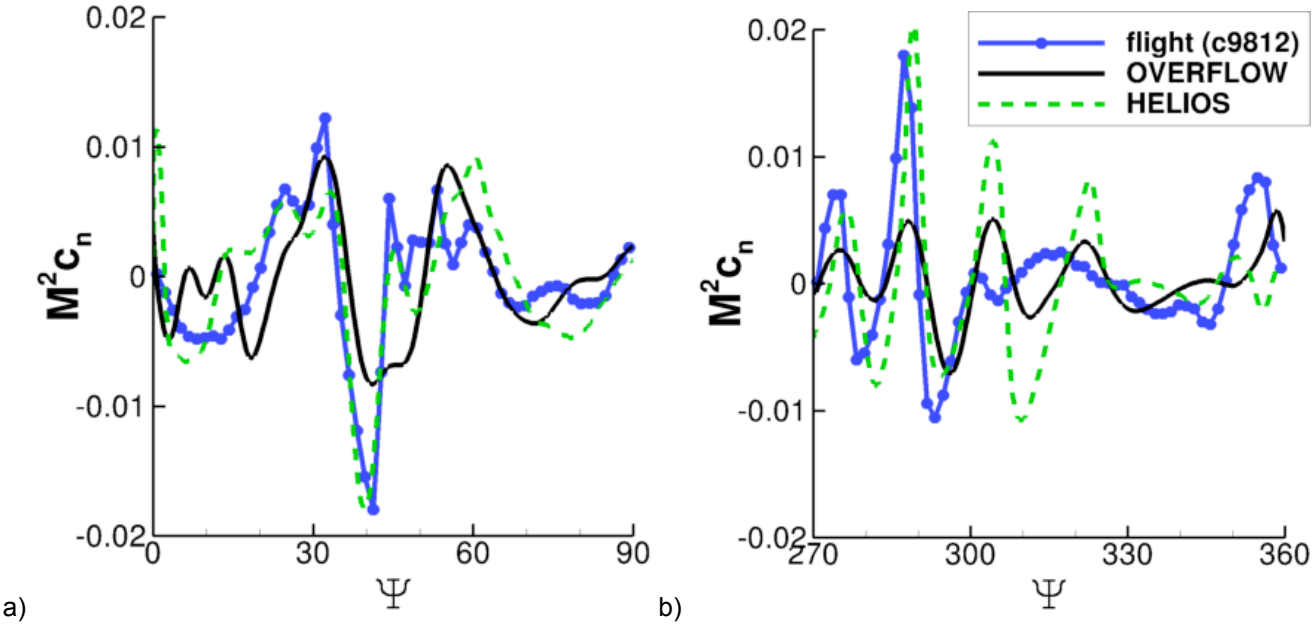

Figure 21. UH-60A descending flight blade-vortex interaction (c9812) normal force 10+/rev airloads, r/R = 0.865: a) advancing side, b) retreating side

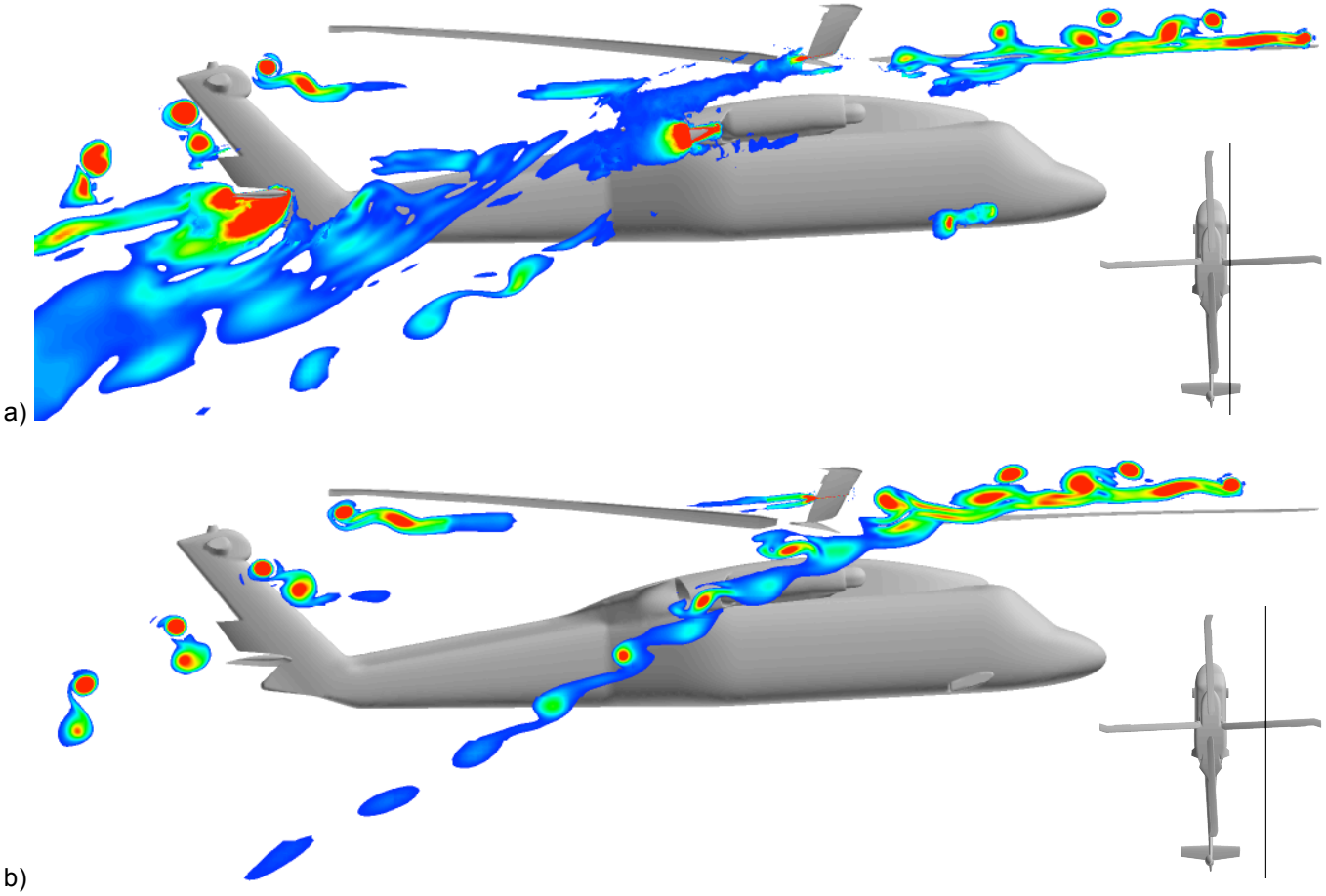

Figure 22. UH-60A low speed (c8515) rotor-fuselage wake-empennage interaction, vorticity contours: a) horizontal tail mid-span, b) rotor mid-span

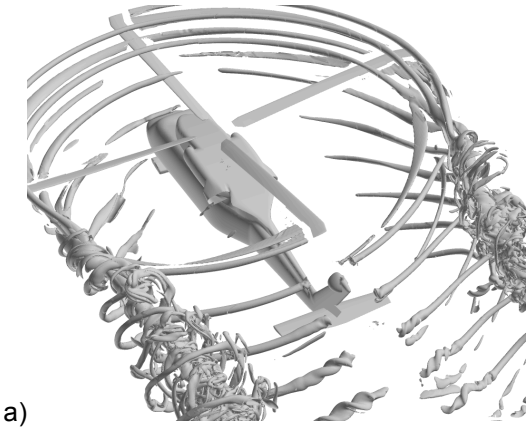

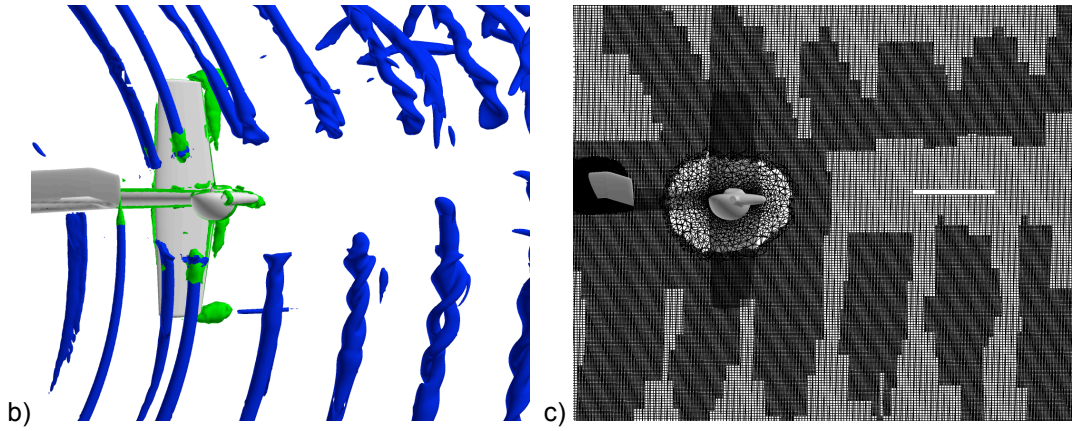

Figure 23. UH-60A low speed (c8515) rotor-fuselage wake-empennage interaction: a) vorticity iso-surface, b) empennage (top-view) vorticity iso-surface, green – near-body, blue-off-body, c) near-body unstructured and off-body AMR grids